DISSERTATION

PATTERN FORMATION IN REACTION DIFFUSION SYSTEMS AND ION

BOMBARDMENT OF SURFACES

Submitted by

Bahaudin A. Hashmi

Department of Mathematics

In partial fulfillment of the requirements

For the Degree of Doctor of Philosophy

Colorado State University

Fort Collins, Colorado

Summer 2017

Doctoral Committee:

    Advisor: Patrick D. Shipman
    Co-Advisor: Jiangguo (James) Liu

    Stephen Thompson
    Daniel J. Bates

ABSTRACT

PATTERN FORMATION IN REACTION DIFFUSION SYSTEMS AND ION

BOMBARDMENT OF SURFACES

We have analyzed pattern formation in two different systems: (1) Vapor-to-particle reaction diffusion systems and (2) Highly ordered square arrays in ion bombardment. The vapor-to-particle reaction exhibits oscillatory behavior and produces a spatial pattern called Liesegang rings. In this thesis, we develop a finite element scheme to model the hydrogen chloride and ammonia vapor-to-particle reaction. In our simulations, we develop parametric regions for different patterns and corroborate data obtained from experiments of this reaction.

For the ion bombardment of a planar surface, we add the Ehrlich-Schwoebel barrier terms to the Bradley-Shipman equations of motion and see the impact of ion bombardment at normal incidence on a binary crystalline material. A weakly nonlinear stability analysis was conducted and regions were determined where highly ordered square pyramids formed.

TABLE OF CONTENTS

Chapter 1

Introduction

This thesis concerns nonlinear partial differential equation models for chemical and physical systems. The models are motivated by experiments. Analysis of the models includes multiple-scale asymptotic analysis and finite-element numerical simulations. The various models can be categorized into two main themes: (1) The vapor-to-particle nucleation and growth of the hydrogen chloride and ammonia reaction, and (2) the formation of highly ordered square patterns in the ion bombardment of a binary crystalline material.

If vapor-phase hydrogen chloride and ammonia are introduced into a tube, after some time the reaction will produce a white solid, ammonium chloride. However, under certain conditions, the diffusion and reaction of these vapor reactants produce precipitary patterns. These patterns are products of precipitary oscillations in the reaction front. We improve on current models by introducing a continuous nucleation differential equation with explicit terms for nucleation and growth kinetics. They include oscillations of varying frequency and amplitude that have been quantified in recent experiments [1] but have not been noticed in previous literature on precipitary reactions. Our simulations are conducted in both one and two dimensions. By analyzing reaction front oscillations we propose the existence of three types of pattern states, one of which has not been observed experimentally.

The second area of interest is the ion bombardment of a binary crystalline material. We extend the Bradley-Shipman model to incorporate the crystalline nature of the bombarded surface. The Bradley-Shipman equations couple surface erosion of a binary material from ion bombardment with surface composition. We add terms pertaining to the Ehrlich-Schwoebel barrier that are derived from the crystalline structure of the material. We conduct a linear stability analysis and define regions in the parameter space that predict the formation of various patterns. We demonstrate that the crystallinity of the material and its binary alloy composition are necessary conditions for the

formation of highly ordered square arrays. This work has resulted in a publication in *Physical Review E* [2].

In Chapter 2, we discuss previous models for nucleation and growth and present our model for the vapor-to-particle reaction of hydrogen chloride and ammonia. In Chapter 3, we discuss the numerical techniques employed for simulating the vapor-to-particle reaction. The results of simulations for this system are presented in Chapter 4. Chapter 5 explains the formation of highly ordered squares under ion bombardment, followed by a discussion on soft mode and defect formation in Section 5.7.

Chapter 2

Oscillations in Reaction-Diffusion Systems

2.1   Introduction

In 1896, Raphael Liesegang mixed inorganic salts in a gel matrix and observed the formation of periodic precipitary bands. It was not a trivial result given that reactant molecules were in a constant change of random motion. More peculiar was the fact that these periodic precipitary bands, known as Liesegang rings, were reproducible in different reactions, under varying scenarios. As the discovery of more diverse patterns continued amongst chemists, the importance of structured pattern formation intrigued scientists from different sciences. Einstein was able to quantify random motion and subsequently developed parabolic partial differential equations for diffusion [3]. A few decades later, Alan Turing in a paper title '*The Chemical Basis of Morphogenesis*' [4] showed that structured patterns can emerge from the 'instability of the homogeneous equilibrium', triggered by 'random disturbances'. Turing showed that by a relatively simple reaction-diffusion model of morphogens, the formation of spots and stripes in nature could be explained. Although Turing's work on mathematical biology was largely ignored and the importance of it dismissed even by Turing himself, his work was reexamined decades later and is now a basis of mathematical understanding in biology.

With the foundation of reaction-diffusion models now on firm footing, scientists have revisited pattern formation in the original chemical reactions. It is now believed that the process that governs Liesegang rings is far more prevalent than previously thought. Many geological formations are believed to arise from similar processes, and recently a link between Balo's sclerosis and periodic precipitation has caused biologists to focus on the chemical kinetics of Liesegang ring formation [5]. In the paper by Thompson and Shipman [6], the vapor-to-particle reaction produced micro weather patterns like tornadoes and hurricanes. In a larger context, organizations like NASA and CERN are conducting research on the effect of aerosols on global weather patterns.
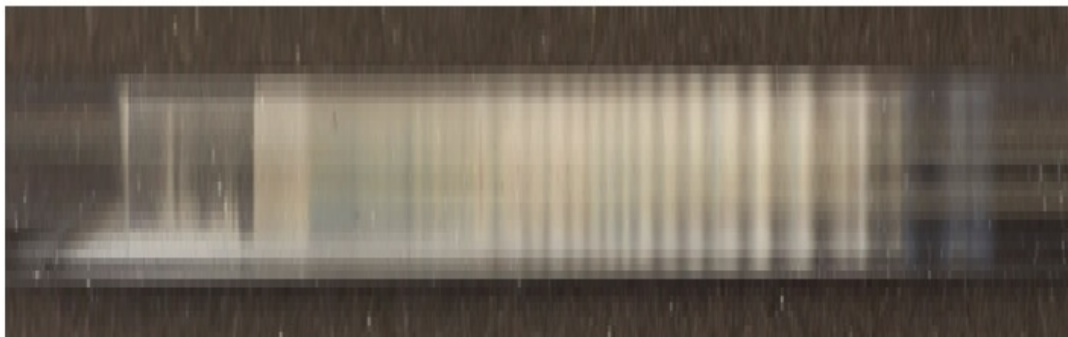
Figure 2.1: Experiment: Vapor-to-particle reaction of hydrogen chloride and ammonia producing Liesegang rings in a reaction tube.

Since the discovery of the Liesegang rings, many theories have been presented in order to understand the chemical kinetics better. The classical understanding of this process, first proposed by Otswald, was based on the concept of local supersaturation i.e. once the concentration of the vapor product of two reactants is greater than a threshold value, the vapor product nucleates to a precipitate by depleting the vapor from its surroundings. As the reaction front moves, it takes time to reach the threshold concentration value again and for the same process to repeat. Hence, *periodic bands of precipitate* (rings) are said to occur discontinuously (see Fig. 2.1[1]). This is known as the prenucleation theory, and most models have adopted it to explain the Liesegang ring phenomenon.

However, recently a detailed analysis of the reaction front have been conducted. It has been observed that the precipitate at the reaction front exhibits oscillatory behavior. It is now our understanding that the Liesegang ring phenomenon is just a special case of this oscillatory pattern. These oscillations have been quantified in [1] and discussed in [6]. In this thesis, essentially we want to develop a model that reflect reaction front oscillations and corroborate experimental data detailed in the vapor-to-particle reaction of ammonia and hydrogen chloride as detailed in [1].

---

[1] Image taken from *Patterns, Oscillations, and Microtornadoes: Extreme Events in Vapor-to-particle Reaction Zones by Thompson and Shipman [6]*

Cotton soaked in
ammonia

Cotton soaked in
hydrogen chloride

Ammonium chloride
precipitate formation
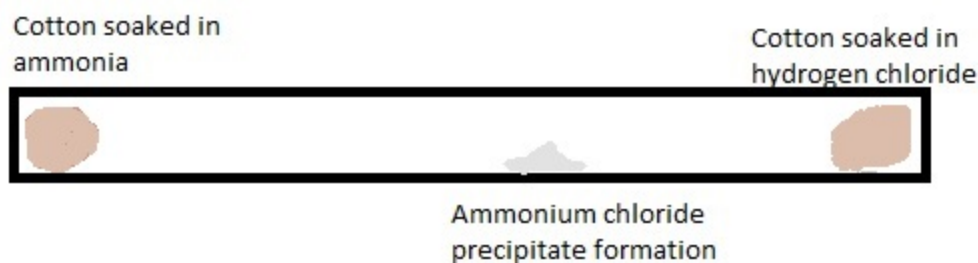
Figure 2.2: Reaction of ammonia and hydrogen chloride

In Chapter 2.2 we lay down the framework for the results that will be presented in Chapter 4. We talk about patterns in vapor-to-particle system as special cases of oscillations in the reaction front. We describe some previous mathematical models used and how we have improved on them to develop our own results.

2.2   Oscillations in Vapor-to-Particle Systems

The ammonia and hydrogen chloride is a classic chemical experiment. It is often used to demonstrate the relative diffusion of chemicals based on their molar mass. In a typical experiment in a reaction tube, ammonia and hydrogen chloride are introduced at opposite ends of the tube and allowed to diffuse (Fig. 2.2). Ammonium chloride precipitate first becomes visible closer to the tube end where hydrogen chloride was introduced. That is because hydrogen chloride has a higher relative molar mass compared to ammonia.

The reaction represented in Fig. 2.2 can be expressed in relative simple terms by the following chemical equation:

$$\mathrm{NH_{3(g)} + HCl_{(g)} \longrightarrow NH_4Cl_{(s)}}$$
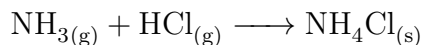
However, there are many intermediates steps that take place before the ammonium chloride precipitate is formed. We describe them in detail in the following section.

2.2.1 HCL-NH$_3$ Reaction

In this section we will explain the hydrogen chloride-ammonia reaction in a way that is consistent with the mathematical model that we will subsequently develop. As a result, many assumptions are made and reaction methodologies proposed in [7–14] and reaction steps detailed in [6] are simplified in the formation of our mathematical model.

The first step in the vapor-to-particle reaction of hydrogen chloride and ammonia is the formation of ammonium chloride vapor. The reaction can be given the following way:

$$\text{NH}_{3(\text{g})} + \text{HCl}_{(\text{g})} \xrightarrow{\text{k}} \text{NH}_4\text{Cl}_{(\text{g})}$$
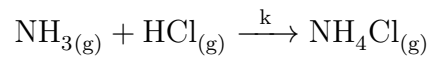
k is the reaction rate constant associated with this reaction. It must be noted at this point that k is a large unknown in scientific circles and there are many parameters that affect k. For example, the affect of water vapor on k is detailed in [15, 16]. In our mathematical model, we assume k to be constant through the entirety of each simulation, however k is varied to obtain simulation data that corroborates experimental data obtained in [1].

The next step involves the formation of ammonium chloride precipitate from ammonium chloride vapor. Chemically it can be written as:

$$\text{NH}_4\text{HCl}_{(\text{g})} \xrightarrow{f} \text{NH}_4\text{Cl}_{(\text{s})}$$
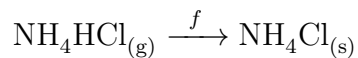
f represents the nucleation and growth rate corresponding to this chemical step. The value of f is dependent on multiple factors and varies throughout the course of a reaction. There have been many proposed versions of f in part literature [6, 17]. We develop a new function that is based on types of nucleation processes:

- Homogeneous nucleation

- Heterogeneous nucleation

In the absence of any catalyst, the formation of ammonium chloride precipitate ($NH_4Cl_{(s)}$) from ammonium chlorde vapor ($NH_4Cl_{(g)}$) will only take place if the concentration value of ammonium chloride vapor is above a threshold value. This is known as homogeneous nucleation. However, if ammonium chloride precipitate is already formed, it acts as a catalyst and the threshold value for further nucleation is reduced. This is called heterogeneous nucleation[2]. The minimum threshold requirement for homogeneous and heterogeneous nucleation have been calculated in [6] and we use them in the constructing the threshold function f.

2.2.2   Saturated-Vapor Reactions: Experiments and Data

There are two types of experiments we analyze: (1) Saturated-vapor experiments and (2) Counter-diffusional experiments. In saturated-vapor experiments, the reaction tube is flooded with one of the reactants until it reaches an equilibrium. The second reactant is then introduced from one of the ends. As a result, the reaction begins immediately at the end of the tube where the second reactant is introduced. A counter-diffusional experiment is similar to the experiment described in Fig. 2.2. Initially, the reaction tube is devoid of each reactant. The reactants are then introduced simultaneously from each end and allowed to diffuse.

We will first discuss saturated-vapor experiments. In particular, we will be discussing the experiments conducted and results obtained by Timothy Lenczycki in [1]. In [1], the author describes the process of conducting saturated-vapor experiments between ammonia and hydrogen chloride. The reaction is conducted in a $20cm$ tube. The tube is then flooded at $77mm/HG$ of hydrogen chloride vapor. Once the entire tube reaches an equilibrium concentration value, ammonia vapor is allowed to diffuse into the tube from one end. An illustration of the experimental set up is given by Fig. 2.3[3].

---

[2]In actual experiments, dust particles in the reaction tube act as catalysts in the vapor-to-particle reaction and hence the phenomenon of heterogeneous nucleation is observed before the process of homogeneous nucleation. In our mathematical model we ignore this aspect and as a result, in our simulations heterogeneous nucleation always takes place after homogeneous.

[3]Image taken from '*Oscillations in gas-phase periodic precipitation patterns: NH_3-HCl Story*' [1]
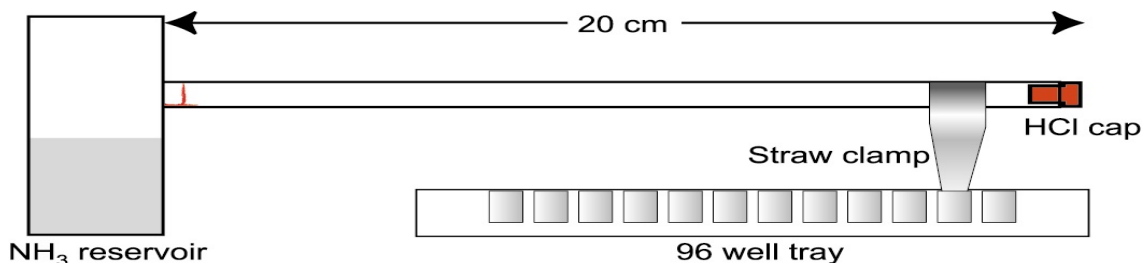
Figure 2.3: Experimental set up for the saturated-vapor reaction of ammonia and hydrogen chloride

When the molecules of ammonia vapor diffuse into hydrogen chloride, a reaction front is immediately established. Due to the pressure vapor differentials of the reactant vapor sources, the reaction front moves down the tube from the initial point of reaction. Eventually, the reaction front position reaches an equilibrium towards the center of the tube. In unprecedented work, the author observed and quantified oscillations in the precipitary deposition at the reaction front as it propelled across the tube. The frequency and amplitude of the precipitary oscillations were calculated and two distinct results were determined: (1) The amplitude of oscillations increased with time and (2) the frequency of oscillations decreased with time. Figs.2.4-2.5 illustrate the two results obtained from experimental data. It must be noted at this point that such oscillations in vapor-to-particle reactions have not been observed before and simulating the data as illustrated in Figs. 2.4-2.5[4] is the primary objective of our reaction-diffusion simulations. With the introduction of a continuous threshold function we present our simulations in Chapter 4. We also demonstrate that the formation of Liesegang rings is a special case of oscillations observed in vapor-to-particle systems. We use the data in [1], to determine values of unknown parameters in our system and demonstrate how varying certain parameter values can lead to different types of pattern formations.

---

[4]Image taken from [1]

Evolution of the Oscillating Front

Top-left plot:
$y = 1.4210\mathrm{E}\text{-}01x + 4.4005\mathrm{E}\text{+}01$
$r^2 = 9.9972\mathrm{E}\text{-}01$

Top-right plot:
$y = 9.4554\mathrm{E}\text{-}02x + 5.5790\mathrm{E}\text{+}01$
$r^2 = 9.9953\mathrm{E}\text{-}01$

Bottom-left plot:
$y = 6.5864\mathrm{E}\text{-}02x + 6.1092\mathrm{E}\text{+}01$
$r^2 = 9.9923\mathrm{E}\text{-}01$

Bottom-right plot:
$y = 4.8210\mathrm{E}\text{-}02x + 7.3456\mathrm{E}\text{+}01$
$r^2 = 9.9477\mathrm{E}\text{-}01$
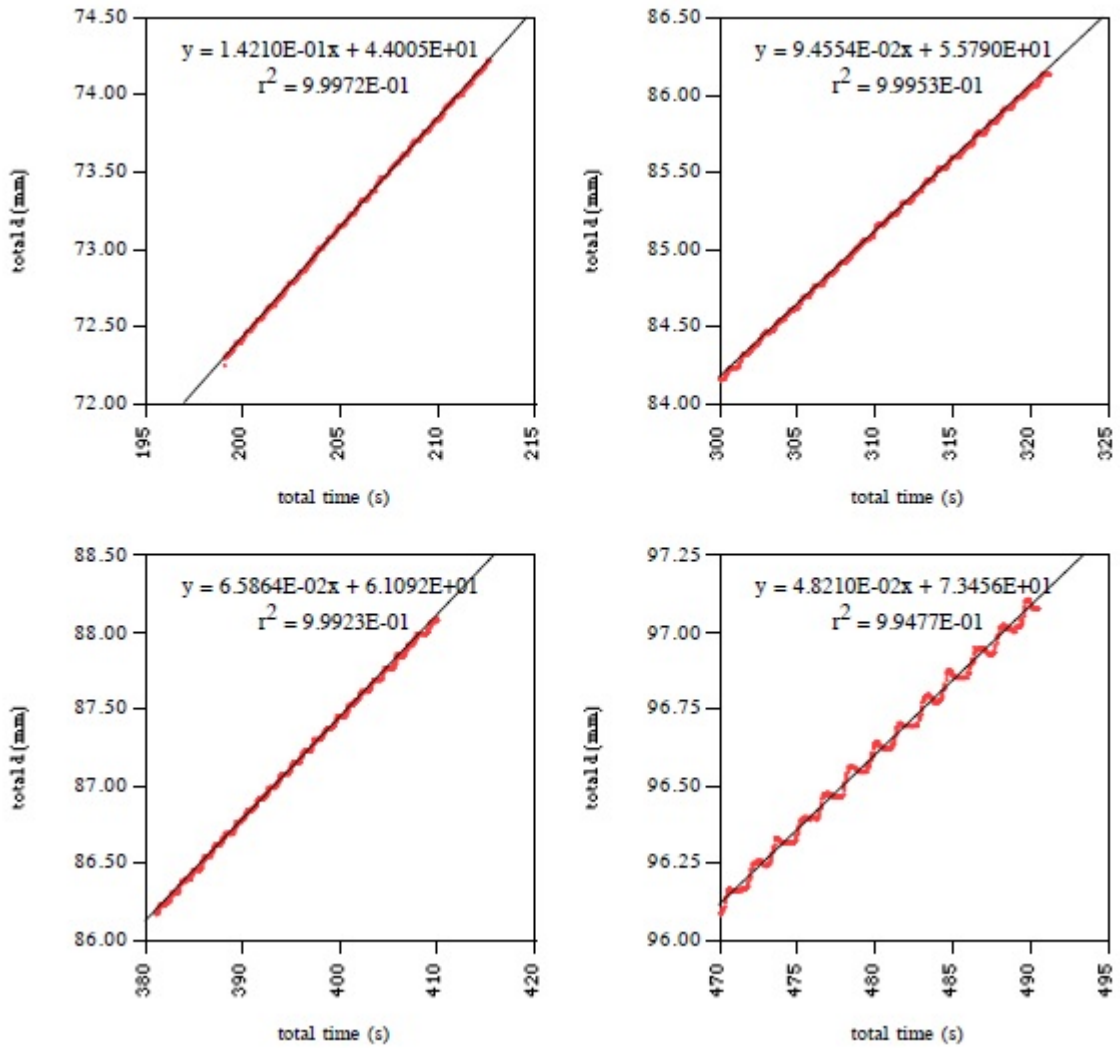
Figure 2.4: Increasing amplitude of precipitary oscillations at the reaction front with time.
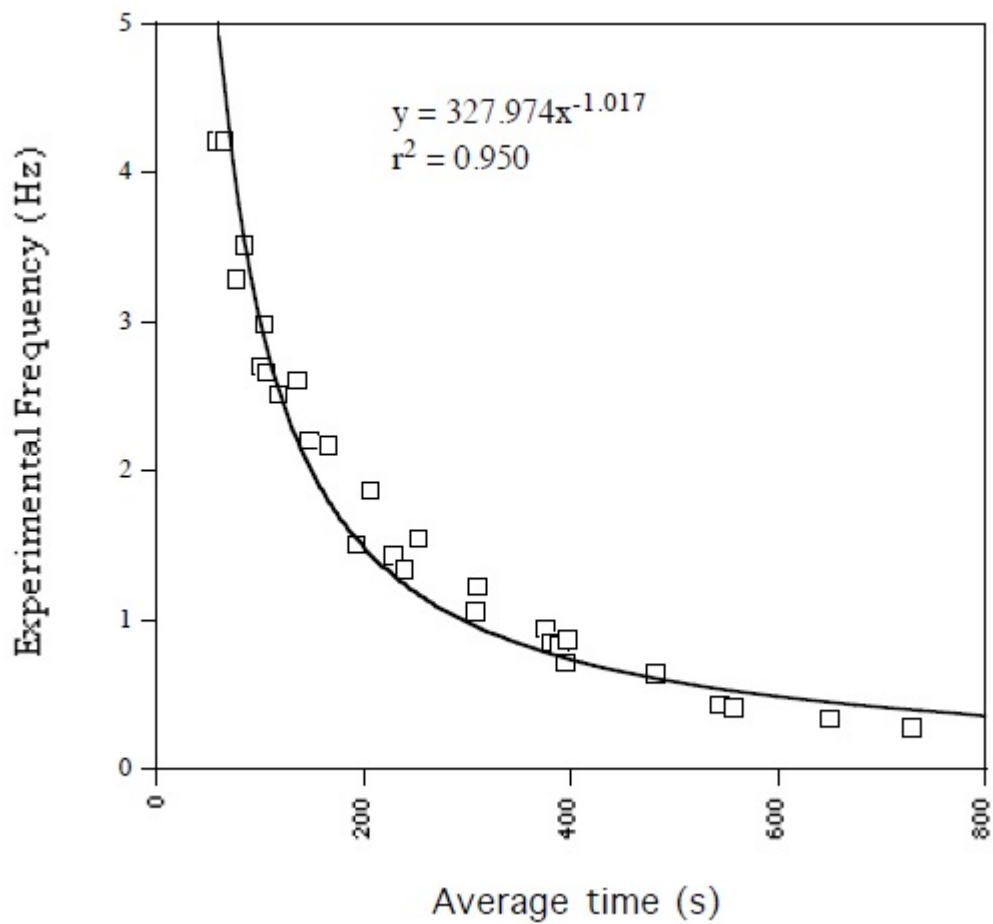
Figure 2.5: Decreasing frequency of precipitary oscillations at the reaction front with time.

2.2.3   Counter-Diffusional Experiments

In counter-diffusional experiments, the reaction tube is initially empty of both reactants. The reactants are then introduced simultaneously from opposite ends and allowed to diffuse through the reaction tube. An illustration of a counter-diffusional experiment is given in Fig. 2.2.

Although, the simulations of counter-diffusional experiments are not the primary objective of this thesis, counter-diffusional have produced extreme micro-weather systems as observed by Thompson and Shipman [6]. We discuss this paper in more detail in section 2.2.4.

2.2.4   Past Mathematical Models

Although, a model has not been previously developed for saturated-vapor, vapor-to-particle ammonia-hydrogen chloride reactions, we analyze the mathematical models proposed for similar reaction-diffusion systems. We will primarily present the work of G.T Dee [18], Keller and Rubinow [19] and Thompson and Shipman [6].

G.T Dee

The model proposed by Dee [18] is concerned with the reaction between hydrogen chloride and silver nitrate suspended in aqueous gel. Dee models saturated-vapor experiments where one of this reactants is allowed to reach equilibrium in the reaction tube before the other reactant is introduced. The basis of Dee's model is the prenucleation theory and requires a little more attention as he has detailed his system in great mathematical detail. In Eq. (2.1), he defines the nucleation rate $J(s)$ as a product of the number of critical nuclei $N(s)$ and the rate at which droplets attach themselves to critical nuclei $\tau(s)$. 's' is the supersaturation ratio. The threshold function that Dee gives is the following,

$$J(s) = N(s)\tau(s) \tag{2.1}$$

where,

$$N(s) = C_0(1+s)exp(-4\pi\sigma r^2/3k_BT)$$

and

$$\tau(s) = (D_3/d^2)[4\pi r^2 dC_0(1+s)]$$

where C_0, σ, r, k_B, T, D_3 and d are parameter values explained in the paper [18].

Dee's model focuses on the *droplet-growth* kinetics pertaining to the prenucleation theory. The size of the droplet affects the nucleation rate at which surrounding smaller droplets get attracted to it. Dee presents the rate of nucleation as a product of the number of critical nuclei (N) and the rate at which droplets attach themselves to a critical nuclei τ. It is known that both N and τ are functions of the supersaturation ratio, hence the rate of nucleation is also a function of s. There are two important conclusions that are reached in Dee's model: (1) Pattern formation is dependent on a rapidly changing threshold function and (2) Precipitate exists between the bands. These are two conclusions that are corroborated in our simulations with a different threshold function but an essential detail that has been overlooked in Dee's work is that fundamental to both his conclusions is the fact that he is modeling an oscillatory system. In our simulations in Chapter 4, we illustrate and quantify these oscillations at the reaction front.

Keller and Rubinow

In the model presented by Keller and Rubinow [19], the nucleation rate is not only dependent on the supersaturation ration but also on the precipitate. The threshold kinetic function presented by Keller and Rubinow is,

$$f_2(a,b,c,d) = \begin{cases} 0 & \text{if } c \le g(d), \\ c - g(d) & \text{if } c > g(d). \end{cases} \tag{2.2}$$

where,

$$g(d) = \begin{cases} c_s > 0 & \text{for } d > 0, \\ c_{ss} > c_s & \text{for } d = 0. \end{cases}$$

In our attempt to use the concept presented by Keller and Rubinow, we develop a continuous form of Eq. (2.2). It is an improvement of Dee's analysis as we not only describe the sink term as a function of the local supersaturation but of also of the precipitate. In [19], the authors demonstrate how the formation of Liesegang bands follow the spacing and time laws of Liesegang rings. In our simulations, the Liesegang bands that do form within a certain parametric region are also in sync with the spacing and time laws. However, in the model proposed by Keller and Rubinow, precipitate does not form in between bands, in contrast to the conclusion reached by Dee [18]. By proposing a continuous threshold function for Eq. 2.2, we bridge the gap between the work of Dee and Keller and Rubinow.

Thompson and Shipman

In the paper *Patterns, oscillations, and microtornadoes: Extreme event in vapor-to-particle reaction zones* [6] by Thompson and Shipman, an analysis of counter-diffusional and saturated-vapor experiments is discussed in relation to the vapor-to-particle reaction of ammonia and hydrogen chloride. The vapor-to-particle reaction of ammonia and hydrogen chloride has produced interesting thermodynamic behaviors like micro-tornadoes and mini-hurricanes in a lab environment. In [6], these processes are explored in great detail. These events primarily take place because of the highly exothermic nature of the reaction. Thompson and Shipman [6] use the prenucleation theory as the basis of their model, while expanding on the Keller-Rubinow [19] model of threshold kinetics. These unique events were a result of counter-diffusional experiments between ammonia and hydrogen chloride. Some of the parameters in our threshold nucleation function have been derived from this paper. We expand on those results to determine a continuous threshold kinetic function which incorporates some of the quantitatively determined parameter values. Later work on this thesis would encompass some of the observations seen in the experiments conducted in this paper [6]. Although the paper does discuss the case when the reaction is conducted in a saturated-vapor experiment, most of the paper reflects on the results when the position of the hydrogen chloride and ammonia drops are varied in a petri dish. The exothermic nature of this particular reaction generates convection currents which leads to extreme weather behavior.

2.3 Mathematical Model

2.3.1 A Model of Partial Differential Equations

Since our system is the typical reaction-diffusion equation, it is modeled by a system of parabolic partial differential equations. For clarification, hydrogen chloride and ammonia are the reactants, the product ammonium chloride in vapor form is called the monomer and the product ammonium chloride in solid form is called the precipitate.

In Eq. (2.3), a represents hydrogen chloride, b represents ammonia, c represents the monomer and d represents the precipitate. As illustrated in Eq. (2.3), a, b and c are modeled by parabolic PDEs while d is modeled by a simple ordinary differential equation as we assume the precipitate to not diffuse in space.

$$
\begin{aligned}
\frac{\partial a}{\partial t} &= D_a \nabla^2 a - kab - f_1(a, b, c, d) \\
\frac{\partial b}{\partial t} &= D_b \nabla^2 b - kab - f_1(a, b, c, d) \\
\frac{\partial c}{\partial t} &= D_c \nabla^2 c + kab - f_2(a, b, c, d) \\
\frac{\partial d}{\partial t} &= \qquad\qquad\quad f_2(a, b, c, d)
\end{aligned}
\tag{2.3}
$$

The main focus in this otherwise traditional model are the terms f_1 and f_2. These terms are responsible for threshold kinetics. But for the sake of simplicity we assume that the reactants do not have an effect on the nucleation threshold and hence we can decouple the system. In our resulting model, $f_1 = 0$ and f_2 becomes a function dependent on just the monomer and precipitate. Hence, we reduce our system to the following chemical process:

$$
a_{(g)} + b_{(g)} \longrightarrow c_{(g)}
$$

$$
c_{(g)} \longrightarrow d_{(s)}
$$
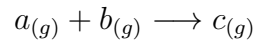
Under these assumptions, mathematically we can write Eq. (2.3) as a system of equations expressed in Eq. (2.4). As we are now only dealing with one type of threshold function, we denote it by just $f(c, d)$. All units of concentration are given in g/cm^3. D_a, D_b, D_c represent the diffusion coefficients of hydrogen chloride, ammonia and ammonium chloride respectively. The mathematical equation modeling the system is as follows:

$$
\begin{aligned}
\frac{\partial a}{\partial t} &= D_a \nabla^2 a - kab \\
\frac{\partial b}{\partial t} &= D_b \nabla^2 b - kab \\
\frac{\partial c}{\partial t} &= D_c \nabla^2 c + kab - f(c, d) \\
\frac{\partial d}{\partial t} &= f(c, d)
\end{aligned}
\tag{2.4}
$$

2.3.2 Threshold Kinetics

The real debate in the modeling of this problem is in determining the appropriate threshold function $f(c, d)$. As mentioned in the literature review previously, there have been many attempts to determine the appropriate right-hand side function. We base our threshold function $f(c, d)$ on the equation proposed by Keller and Rubinow in Eq. (2.2). The nucleation process is based on threshold kinetics. The precipitate does not form unless the concentration of the monomer is above a certain threshold value, c_{hom}. However, once precipitate exists at a point, the threshold concentration for further nucleation is reduced and precipitate will form at lower concentration values of the monomer.

In all the simulations we have conducted, $c_{hom} = 0.02$ and $c_{het} = 0.002$. These values are based on the paper by Thompson and Shipman [6]. The threshold function is

$$
f(c, d) = \frac{\kappa(c + \phi - \gamma e^{-d})^{\eta+1}}{1 + (c + \phi - \gamma e^{-d})^{\eta}},
\tag{2.5}
$$

where
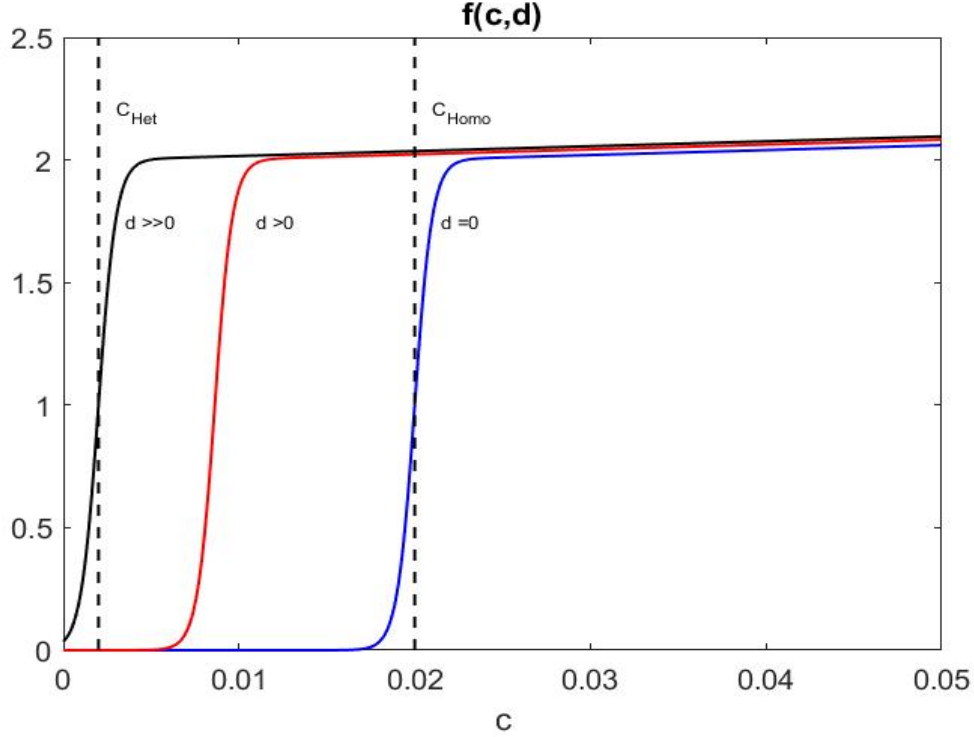
Figure 2.6: Effect of precipitate d on the threshold function $f(c,d)$ with $c_{hom} = 0.02$, $c_{het} = 0.002$, $\kappa = 2$ and $\eta = 10000$.

$$\phi = 1 - c_{het} \text{ , and}$$

$$\gamma = c_{hom} - c_{het}.$$

We have assumed the threshold function to decrease exponentially with the increase in the precipitate. c_{het} represents the minimum value required for nucleation to take place. The threshold dynamics are illustrated in Fig. 2.6. The benefit of this equation is we have explicit terms for homogeneous and heterogeneous nucleation.

2.3.3 Boundary and Initial Conditions

Apart from trying to determine the appropriate threshold function representing Eq. (2.2), for our simulations we will vary a few parameters. Amongst those, different boundary and initial conditions play an important role in simulating different classes of experiments. Despite tubes being three dimensional objects, we assume our system to be in either one or two dimension. So

for our simulations, our boundary conditions are concentrations at the extreme end points of the tube. In the case of the one dimensional system the boundary conditions are expressed Eq. (2.6).

$$
\begin{aligned}
a(0,t) &= a_o, & b(0,t) &= b_o \\
\frac{\partial a}{\partial x}(L,t) &= 0, & \frac{\partial b}{\partial x}(0,t) &= 0 \\
\frac{\partial c}{\partial x}(0,t) &= 0, & \frac{\partial c}{\partial x}(L,t) &= 0 \\
\frac{\partial d}{\partial x}(0,t) &= 0, & \frac{\partial d}{\partial x}(L,t) &= 0.
\end{aligned}
\tag{2.6}
$$

In the two types of experiments that are conducted, the boundary conditions remain qualitatively the same i.e. a_0 and b_0 are both non-negative values in the counter-diffusional model and the saturated-vapor model.

The initial conditions however, are different for the two experiments. In the case of the counter-diffusional experiment in Eq. (2.7) $a_1 = 0$ and $b_1 = 0$. In the saturated-vapor model, we choose the initial condition of one of the two reactants to be greater than zero. In the lab experiments conducted by Tim Lenczycki [1], the concentration of hydrogen chloride was greater than zero at the beginning of the experiment. The initial conditions are,

$$
\begin{aligned}
a(x,0) &= a_1 \\
b(x,0) &= b_1 \\
c(x,0) &= 0 \\
d(x,0) &= 0.
\end{aligned}
\tag{2.7}
$$

Once the PDE system is set, up we discuss various solution techniques in Chapter 3.

Chapter 3

Numerical Techniques

To solve the mathematical model represented by Eq. (2.4), finite element schemes for one and two dimensional parabolic systems are developed. Our scheme consists of discretizing the spatial and temporal domains. For the spatial discretization, we develop a continuous Galerkin P1 finite element scheme explained in Section 3.1-3.3. In Section 3.4, we use the Crank-Nicholson method to develop the temporal scheme. After solving the partial differential equations in Eq. (2.4), in Section 3.5 we describe our Runge-Kutta scheme for evaluating the only ordinary differential equation in Eq. (2.4). For the following sections, we define our spatial domain be $\Omega = [\Omega_\circ, \Omega_\delta] \in \mathbf{R}^2$, where $\Omega_\circ$ represents the interior of the domain and Ω_δ represents the boundary of the domain. M represents the total number of elements in Ω and N is equal to the total number of time iterations.

3.1   Spatial Discretization: Basis Vectors

To explain our numerical technique, let us begin with an inhomogeneous parabolic partial differential equation as follows:

$$u_t + \triangle u = f \in \Omega \times [0, T] \tag{3.1}$$

If the domain $\Omega \in \mathbf{R}$ (one-dimensional simulation), it is discretized by uniform intervals and if the domain $\Omega \in \mathbf{R}^2$(two-dimensional simulation), it is discretized by triangular elements. The triangular elements are not uniform in size or orientation. A finer mesh is used for areas closer to the boundary.

In order to evaluate Eq. (3.1), we linearize it with piecewise linear functions. For that purpose, let us define the space V_h such that $V_h \subseteq V = H_0^1(\Omega)$, where H_0^1 is the Hilbert space of polynomial degree 1. If $u^h(t) \in V_h$, we can develop a variational form of Eq. (3.1) given by,

18

$$\int_\Omega \dot{u^h} v + \int_\Omega \nabla u^h . \nabla v = \int_\Omega f(t) v \qquad \forall v \in V_h \tag{3.2}$$

At a fixed time $t_n \in [0, T]$, we approximate $\dot{u^h}$ such that $\dot{u^h} = \dfrac{u_n^h - u_{n-1}^h}{\Delta t}$ for $\Delta t = \dfrac{T}{N}$ where N is the total number of time iterations and $u_n^h \approx u(t_n)$. We can now substitute our discretized derivative into Eq. (3.2) to develop the following equation:

$$\int_\Omega \frac{u_n^h - u_{n-1}^h}{\Delta t} v + \int_\Omega \nabla u . \nabla v = \int_\Omega f(t) v \qquad \forall v \in V_h$$

$$\int_\Omega u_n^h v + \Delta t \int_\Omega \nabla u^h . \nabla v = \Delta t \int_\Omega f(t) v + \int_\Omega u_{n-1}^h v \qquad \forall v \in V_h \tag{3.3}$$

From Eq. (3.3) it is obvious that we have to linearize three types of integrals. The matrix corresponding to $\int_\Omega \nabla u . \nabla v$ is called the global stiffness matrix A, for $\int_\Omega u_n^h v$ and $\int_\Omega u_{n-1}^h v$ it is called the global mass matrix B and $\int_\Omega f(t) v$ is represented by the global right-hand side matrix $F(t)$.

We define u^h to be the approximate solution of u given in equation (3.1) and has the following representation:

$$u^h = \sum_{i=1}^{M} \xi_i(t) \varphi_i(x) \tag{3.4}$$

where $\varphi_i \ \forall \ i = 1, 2, .., M$ represent the basis vectors of V_h such that $V_h = span \ [\varphi_1, \varphi_2, ..., \varphi_M]$. If $\Omega \subseteq \mathbf{R}$ (one-Dimensional case) then we define the linear basis functions as follows:

$$\varphi_i(x) = \begin{cases} 0 & \text{if } x \leq x_{i-1}, \\ \dfrac{(x - x_{i-1})}{h} & \text{if } x_{i-1} \leq x < x_i. \\ 1 - \dfrac{(x - x_i)}{h} & \text{if } x_i \leq x < x_{i+1}. \\ 0 & \text{if } x \geq x_{i+1}, \end{cases} \tag{3.5}$$
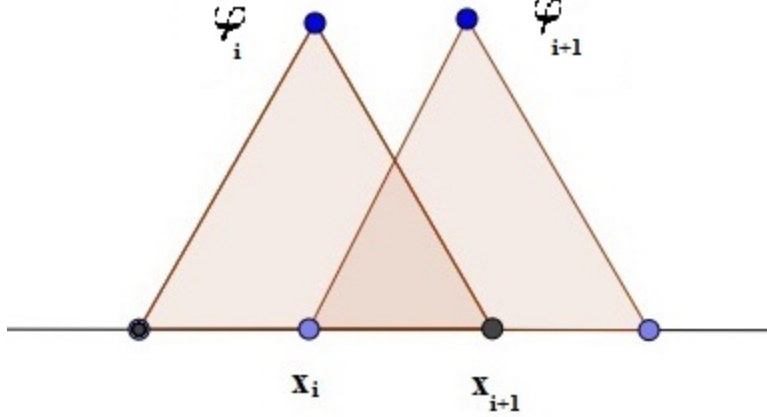
Figure 3.1: Hat function (linear basis function) for One-Dimensional elements

If $\Omega \subseteq \mathbf{R}^2$ (two-dimensional case), we define a node $P_j = (x_j, y_j)$ which represents the coordinates of the jth node of the triangular elements in Ω. Analogous to the one-dimensional linear basis functions defined in Eq. (3.5), we define similar linear basis function for $\Omega \subseteq \mathbf{R}^2$ such that $\varphi_i(P_j) = \begin{bmatrix} 1 & \text{if } i = j \\ 0 & \text{if } i \neq j \end{bmatrix}$. The height of the basis function $\varphi_i(P_i)$ is supported by continuous linear functions $(L(x,y))$ from P_i to all the neighboring nodes as given in Fig. 3.2 such that $L_{ik}(x_i, y_i) = \varphi_i(P_i) = 1$ and $L_{ik}(x_k, y_k) = \varphi_i(P_k) = 0$ where $P_k = (x_k, y_k)$ represents any one of the neighboring nodes of P_i.

3.2 Assembling of Matrices

As mentioned in the previous section, we need to solve for three types of integrals. Since we have also discretized the domain with the appropriate basis functions, we start with the formulation of the global stiffness matrix.

3.2.1 Global Stiffness Matrix:

We have two cases corresponding to the two dimensions in the assembly of the global stiffness matrix. We will first discuss the one-dimensional case before we proceed to the assembly in two-dimension.

20
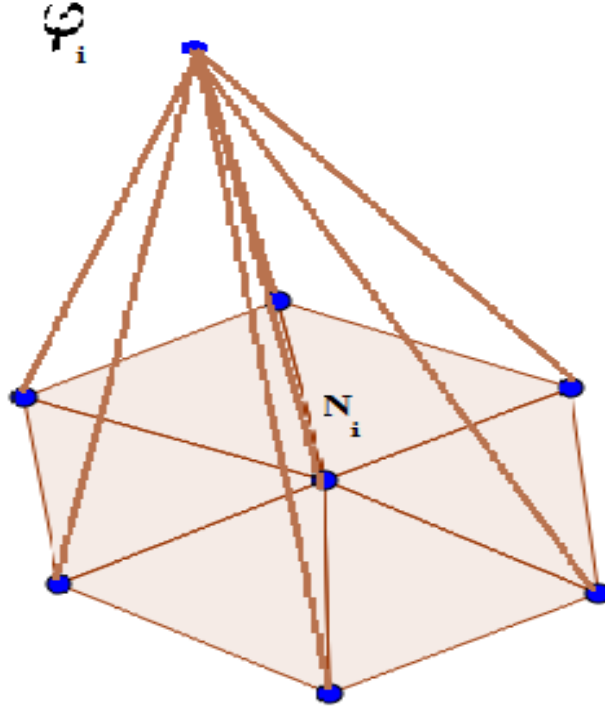
Figure 3.2: Hat function (linear basis function) for 2D triangulation

For the one-dimensional case let the domain be equal to $[0, L]$ where L is the length of our domain. For our own convenience, we partition the domain into N uniform intervals such that the length of each interval E is $h = \dfrac{L}{N}$. As mentioned before, the global stiffness matrix corresponds to the linearization of the divergence term in Eq. (3.3). Hence our global stiffness matrix A can be expressed in the following way:

$$A = \sum_{E \in \Omega} \int_{\Omega} \nabla \varphi_i . \nabla \varphi_j dx \qquad \forall i, j = 1, 2, ..., N \qquad (3.6)$$

Before we sum over all elements to obtain A, let us define our element stiffness matrix M_{ij} such that,

$$M_{ij} = \int_{[0,L]} \nabla \varphi_i . \nabla \varphi_j dx$$

If $j = i + 1$, using Eq. (3.5), it can easily be shown that $M_{ij} = \dfrac{1}{h} \begin{bmatrix} 1 & -1 \\ -1 & 1 \end{bmatrix}$ and hence,

$$A = \frac{1}{h} \begin{bmatrix} 1 & -1 & 0 & 0 & \dots \\ -1 & 2 & -1 & 0 & \dots \\ 0 & -1 & 2 & -1 & \dots \\ 0 & 0 & -1 & 2 & \dots \\ \vdots & \vdots & \vdots & \vdots & \ddots \end{bmatrix}$$

We proceed in a similar fashion to evaluate the global stiffness matrix in two-dimensions, the only difference in our elements E being triangles rather than intervals. Our global stiffness matrix is defined as,

$$A = \sum_{E \in \Omega} \int_{\Omega} \nabla\varphi_i . \nabla\varphi_j dx \qquad \forall i, j = 1, 2, ..., N \qquad (3.7)$$

where N is the total number of triangular elements in our domain. Before we define our basis vectors in two-dimensions, let us define notation for our triangular elements. For a triangular element $E \in \Omega$, let E be defined by the vertices P_i, P_j and P_k. φ_i, φ_j and φ_k are the corresponding basis vectors defined for each of the three vertices. Eq. (3.8) illustrates a convenient form of the basis vector corresponding to P_i.

$$\varphi_i(x, y) = \begin{vmatrix} 1 & 1 & 1 \\ x & x_j & x_k \\ y & y_j & y_k \end{vmatrix} \begin{vmatrix} 1 & 1 & 1 \\ x_i & x_j & x_k \\ y_i & y_j & y_k \end{vmatrix}^{-1} \qquad (3.8)$$

Subsequently, the gradient vector of Eq. (3.8) can be calculated accordingly,

$$\nabla\varphi_i(x, y) = \frac{1}{2|E|} \begin{pmatrix} y_j - y_k \\ x_j - x_k \end{pmatrix}$$

where $2|E| = \begin{vmatrix} x_j - x_i & x_k - x_i \\ y_j - y_i & y_k - y_i \end{vmatrix}$. The resulting element stiffness matrix M_E is,

$$M_E = \begin{bmatrix} M_{ii} & M_{ij} & M_{ik} \\ M_{ji} & M_{jj} & M_{jk} \\ M_{ki} & M_{kj} & M_{kk} \end{bmatrix}$$

where the following equation is used to calculate each elements of M_E

$$M_{jk} = \int_E \nabla\varphi_j.\nabla\varphi_k dx = \frac{|E|}{(2|E|)^2}(y_k - y_i, x_i - x_k)\begin{pmatrix} y_i - y_j \\ x_j - x_i \end{pmatrix} \tag{3.9}$$

We can solve for M_E simultaneously by using the following equation,

$$M_E = \frac{|E|}{2}.GG^T \qquad \text{with } G := \begin{pmatrix} 1 & 1 & 1 \\ x_i & x_j & x_k \\ y_i & y_j & y_k \end{pmatrix}^{-1}\begin{pmatrix} 0 & 0 \\ 1 & 0 \\ 0 & 1 \end{pmatrix} \tag{3.10}$$

With Eq. (3.10), we can now solve for the global stiffness matrix A corresponding to Eq. (3.7).

3.2.2 Global Mass Matrix:

To evaluate the global mass matrix B we follow the same route as in the previous section. We will first explain the calculation in one-dimension before we proceed to two-dimensions. In one-dimension, the global mass matrix B can be expressed as follows,

$$B = \sum_{E \in [0,L]} \int_{[0,L]} \varphi_i\varphi_j dx \qquad \forall i, j = 1, 2, ..., N \tag{3.11}$$

In order to evaluate B, we will first solve for the element mass matrix M_{ij} where,

23

$$M_{ij} = \int_{[0,L]} \varphi_i \varphi_j dx$$

If $j = i + 1$, the corresponding element mass matrix $M_{ij} = \dfrac{h}{6} \begin{bmatrix} 2 & 1 \\ 1 & 2 \end{bmatrix}$ and hence,

$$B = \frac{h}{6} \begin{bmatrix} 2 & 1 & 0 & 0 & \dots \\ 1 & 4 & 1 & 0 & \dots \\ 0 & 1 & 4 & 1 & \dots \\ 0 & 0 & 1 & 4 & \dots \\ \vdots & \vdots & \vdots & \vdots & \ddots \end{bmatrix}$$

If our domain $\Omega \in \mathbf{R}^2$, similar to the methodology used in evaluating our two-dimensional element stiffness matrix, our elemental mass matrix M_E for the triangular element E with vertices P_i, P_j and P_k can be given by,

$$M_E = \frac{1}{24} \begin{vmatrix} x_j - x_i & x_k - x_i \\ y_j - y_i & y_k - y_i \end{vmatrix} \begin{pmatrix} 2 & 1 & 1 \\ 1 & 2 & 1 \\ 1 & 1 & 2 \end{pmatrix} \tag{3.12}$$

Using Eq. (3.11)-(3.12) we can evaluate the global mass matrix B.

3.2.3 Global Right Hand Side and Boundary Conditions

The global right hand side vector $F_n(t)$, corresponds to the term $\int_\Omega f(t)v$ in Eq. (3.3). For an element E defined by nodes P_i, P_j and P_k in our domain we have,

$$\int_E f\varphi_i dx \approx \frac{1}{6} \begin{vmatrix} x_j - x_i & x_k - x_i \\ y_j - y_i & y_k - y_i \end{vmatrix} f_C \tag{3.13}$$

where ,

$$f_C = \frac{1}{3}(f(N_i) + f(N_j) + f(N_k))$$

24

We now have all corresponding matrices to substitute terms in Eq. (3.3). In the next section, we will discuss our implementation of Dirichlet and Neumann boundary conditions.

3.3 Boundary Conditions

In the modeling of the system (2.4), there are two types of boundary conditions that emerge. Before the boundary conditions are expounded upon, we have to detail some notation. We define our domain Ω such that $\Omega = [\Omega_\circ, \Omega_\partial]$, where $\Omega_\circ$ represents the interior of the domain and Ω_∂ represent the boundary. The boundary $\Omega_\partial = [\Omega_\partial^D, \Omega_\partial^N]$ where Ω_∂^D and Ω_∂^N represent parts of the boundary where Dirichlet and Neumann boundary conditions are applied respectively.

For all $k \in [1, 2, ..., M]$ such that $N_k \in \Omega_\partial^N$, we implement the Neumann boundary condition $\dfrac{du_n(N_k)}{d\vec{n}} = 0$ where $\vec{n}$ is the normal vector.

To implement Dirichlet boundary condition if $N_k \in \Omega_\partial^D$ for some $k \in [1, 2, ..., M]$ then we implement the boundary condition on $U_n(N_k) = f^D$ where f^D is the boundary function. In our system of equations f^D is always a constant.

3.4 Temporal Discretization: Backward-Euler and Crank-Nicholson Method

We will now discuss the temporal discretization of the domain. To derive Eq. (3.3) from Eq. (3.1) we used the Backward-Euler method to discretize the derivative u_t such that $u_t = \dfrac{u_n - u_{n-1}}{\Delta t}$ As mentioned before, for our simulations we keep the time steps Δt uniform for all iterations. We implement the Backward-Euler scheme in Eqs. (3.14-3.15).

$$BU_n + dt(AU_n) = \Delta t F_n + BU_{n-1} \tag{3.14}$$

$$U_n = (B + \Delta t(A))^{-1}(\Delta t F_n + U_{n-1}B) \tag{3.15}$$

For the Crank-Nicholson scheme along with the discretization of the derivative in Eq. (3.3, 3.14-3.15), we substitute u_n by its average over t_{n-1} and t_n such that $u_n = \dfrac{u_n + u_{n-1}}{2}$. Our improved version of Eq. (3.3) can be expressed as,

$$\int_\Omega u_n v + \Delta t \int_\Omega \nabla(\frac{u_n + u_{n-1}}{2}).\nabla v = \Delta t \int_\Omega (\frac{f_n(t) + f_{n-1}(t)}{2})v + \int_\Omega u_{n-1}v \qquad (3.16)$$

Linearizing Eq. (3.16), we obtain

$$(B + \frac{\Delta t}{2}A)U_n = (B - \frac{\Delta t}{2}A)U_{n-1} + \Delta t(\frac{F(t_n) + F(t_{n-1})}{2}) \qquad (3.17)$$

$$U_n = (B + \frac{\Delta t}{2}A)^{-1}((B - \frac{\Delta t}{2}A)U_{n-1} + \Delta t(\frac{F(t_n) + F(t_{n-1})}{2})) \qquad (3.18)$$

As our spatial and temporal discretization is complete, we can now apply our numerical techniques to our equations explained in system (2.4).

3.5   Computing Ammonium Chloride Precipitate

In our original system 2.4, we use the finite element scheme described earlier to evaluate for the three parabolic PDEs for hydrogen chloride (a), ammonia (b) and ammonium chloride (c).However, the equation to model ammonium chloride precipitate (d) is a standard ordinary differential equation. For that purpose we use Runge-Kutta scheme of order 4. Our differential equation for ammonium chloride precipitate is given by,

$$d_t = f(c, d) \qquad (3.19)$$

If c_n and d_n are known, we can evaluate for d_{n+1} according to,

$$d_{n+1} = d_n + \frac{\Delta t}{6}(k_1 + k_2 + k_3 + k_4) \qquad (3.20)$$

26

where $k_1 = f(c_n, d_n)$, $k_2 = f(c_n + \frac{\Delta t}{2} k_1, d_n + \frac{\Delta t}{2} k_1)$, $k_3 = f(c_n + \frac{\Delta t}{2} k_1, d_n + \frac{\Delta t}{2} k_2)$ and $k_2 = f(c_n + \frac{\Delta t}{2} k1, d_n + \Delta t k_3)$.

We will now implement our numerical techniques to our system 2.4 and illustrate some of our results in Chapter 4.

Chapter 4

Simulations

4.1 One-Dimensional Simulations

As the threshold function $f(c, d)$ is the base of our reaction-diffusion system, we illustrate simulations corresponding to ammonium chloride vapor and ammonium chloride precipitate. We present the results for varying values of the reaction rate parameter k. The primary reason for that is the reaction rate k not only affects the production rate of ammonium chloride vapor but also affects the structure of the reaction front. Fig. 4.1 demonstrates the affect of the reaction rate on the reaction front. The reaction rate k is a large unknown in scientific circles. Experimental estimates of the reaction range from $10^{-1} \leq k \leq 10^{12}$ [1,6]. It is also not constant under all conditions. The effect of water vapor on the reaction rate has been explored extensively in previous studies [15,16]. In our simulations, smaller values of k have proved to be more effective in corroborating physical data. We still do not have an exact value for the reaction rate k, but based on the correlation between experimental data and our simulations we believe that $10^{-1} \leq k \leq 10^2$.

Although interesting patterns have been observed in our simulations, the foremost purpose of our model is to corroborate some of the experimental observations presented by Tim Lenzycki in [1]. He observes that in a saturated-vapor experiment of hydrogen chloride and ammonia, the amount of precipitate (amplitude) at the reaction front increases with time while the frequency of the oscillations of precipitary deposit decreases with time. In the following illustrations, the monomer has been scaled by a factor of 100 to be more discernible in the figures.

Fig. 4.2 represents the one-dimensional simulation with parameters corresponding to the saturated-vapor experiments in [1]. In Fig. 4.2(a), the reaction front is formed and has reached the concentration threshold for homogeneous nucleation to take place. At $t = 0$, the reaction flux of hydrogen chloride and ammonia are at their maximum value. As a result, the reaction front's velocity is also
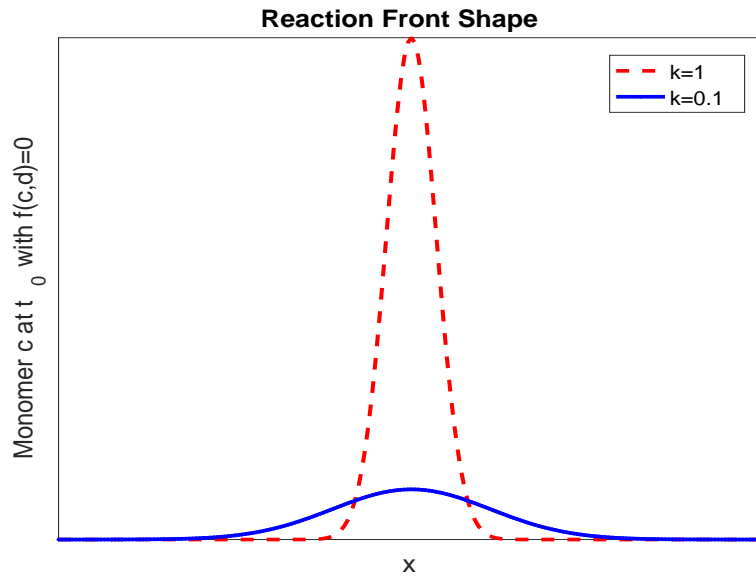
Figure 4.1: Reaction front shape for varying values of the reaction rate k
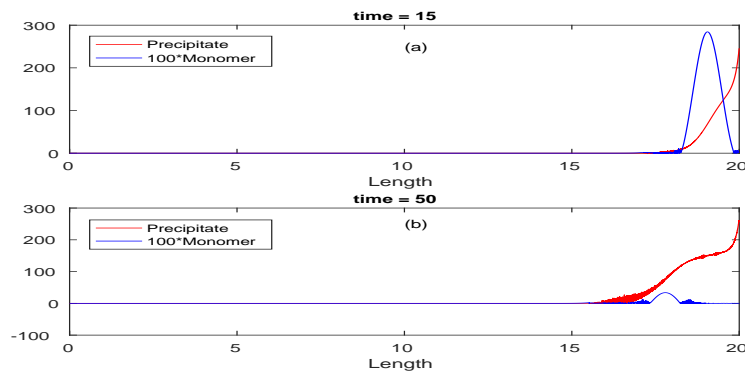
Figure 4.2: Numerical Simualtion: Precipitate in tube with $a_0 = a_1 = 77$, $b_0 = 45$, $b_1 = 0$, $k = 10$, $\kappa = 2$, $\phi = 0.998$, $\gamma = 0.018$ and $\eta = 20000$.
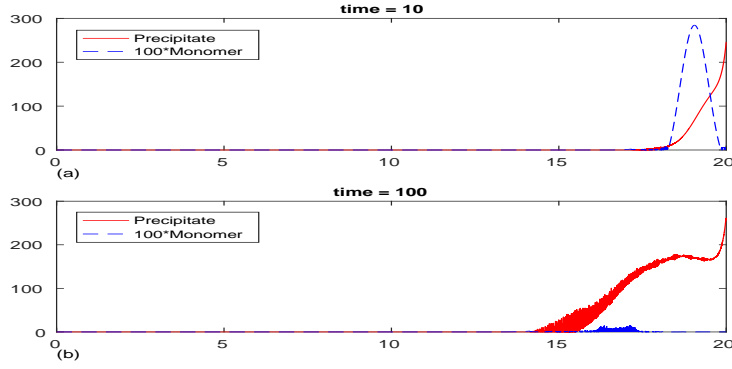
Figure 4.3: Numerical Simulation: Precipitate in tube with $a_0 = a_1 = 77$, $b_0 = 45$, $b_1 = 0$, $k = 0.01$, $\kappa = 2$, $\phi = 0.98$, $\gamma = 0.018$ and $\eta = 20000$.
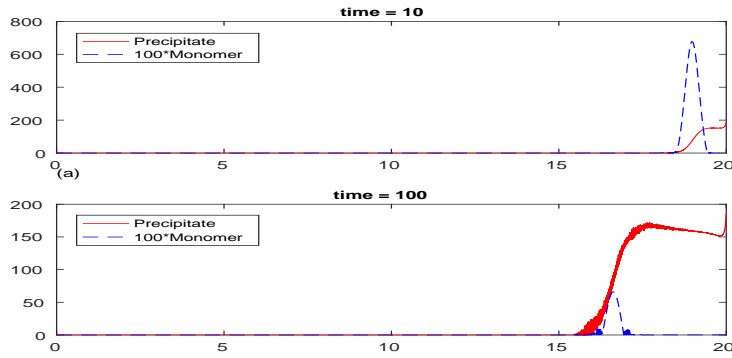
Figure 4.4: Numerical Simulation: Precipitate in tube with $a_0 = a_1 = 77$, $b_0 = 45$, $b_1 = 0$, $k = 1$, $\kappa = 2$, $\phi = 0.98$, $\gamma = 0.018$ and $\eta = 20000$.

at it's largest at the start of the reaction. As the reaction front velocity is reduced, oscillations at the reaction front can be observed. These oscillations are observable in Fig. 4.2(b).

Figs. 4.3-4.5, demonstrate the effect of varying the reaction rates k at the start of the reaction. We can observe in Fig. 4.5 that oscillations are less apparent and the width of the reaction front is smaller compared to the simulations in Figs. 4.4-4.3. This is due to the effect of the reaction rate k on the horizontal spread of the reaction front as illustrated in Fig. 4.1.

Fig. 4.6 shows the results at $t = 300$ for $k = [0.01, 1, 10]$. The reaction front velocity has slowed down considerably and in Fig. 4.6(a)-(d) rings begin to appear for $k = 0.01$ & $k = 1$. In Fig. 4.6(e)-(f), rings are replaced with oscillations due to the higher value of k.
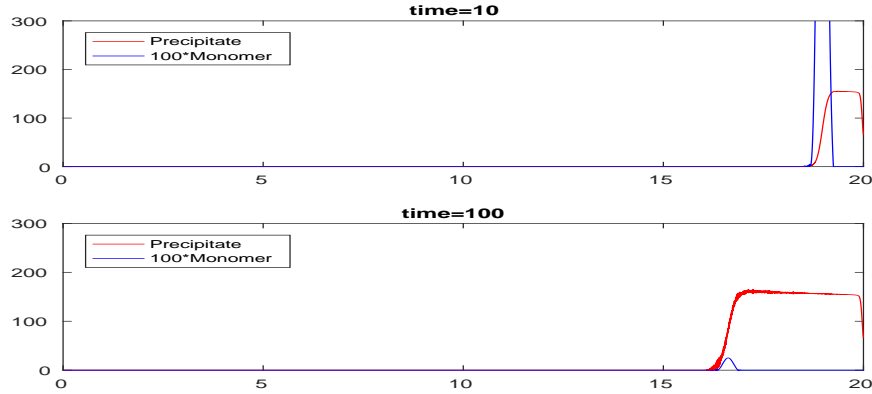
Figure 4.5: Numerical Simulation: Precipitate in tube with $a_0 = a_1 = 77$, $b_0 = 45$, $b_1 = 0$, $k = 10$, $\kappa = 2$, $\phi = 0.998$, $\gamma = 0.018$ and $\eta = 20000$.

A closer look of Fig. 4.6(a)-(b) at $t = 600$ can be seen in Fig. 4.7(a)-(d). In Fig. 4.8(a)-(d), spatially uniform rings appear and in Fig. 4.9 we can observe the change from oscillations to spatially uniform rings. The rings have become more distinct but are irregularly positioned.

In our analysis of the reaction front, we have aimed to replicate Lenczycki's definition of the reaction front and then calculate the corresponding amplitude and frequency. Fig. 4.10 shows the precipitate at the reaction front. The oscillations are clearly visible. Initially, the frequency of these oscillations is hard to determine visually but as the frequency decreases, the period increases and the oscillations become more apparent. This behavior is consistent with observations in [1]. We conduct similar reaction front analysis with different values of k. For any reasonable value of k, there is an increase in amplitude and decrease in frequency as a function of time. However, varying k does affect the formation of rings. Ring formation only take place at the appropriate combination of front velocity and threshold dynamics. That combination is most sensitive to the reaction rate k.

The purpose of illustrating the effect of a changing reaction rate was to demonstrate the dependency of different patterns on the reaction rate parameter. As mentioned in the beginning of this thesis, we believe there are three distinct pattern states in the hydrogen chloride ammonia reaction-diffusion system: (1) Rings that are not spatially uniform (Fig. 4.7 (b) & (d)) (2) Rings that are spatially uniform (Fig. 4.8 (b) & (d)) (3) Precipitary oscillations but no rings (Fig. 4.9 (b) & (d)).

However, to corroborate experimental data provided in [1], we need to demonstrate that precipitary amplitude at the reaction front increases with time while the frequency decreases. The

31
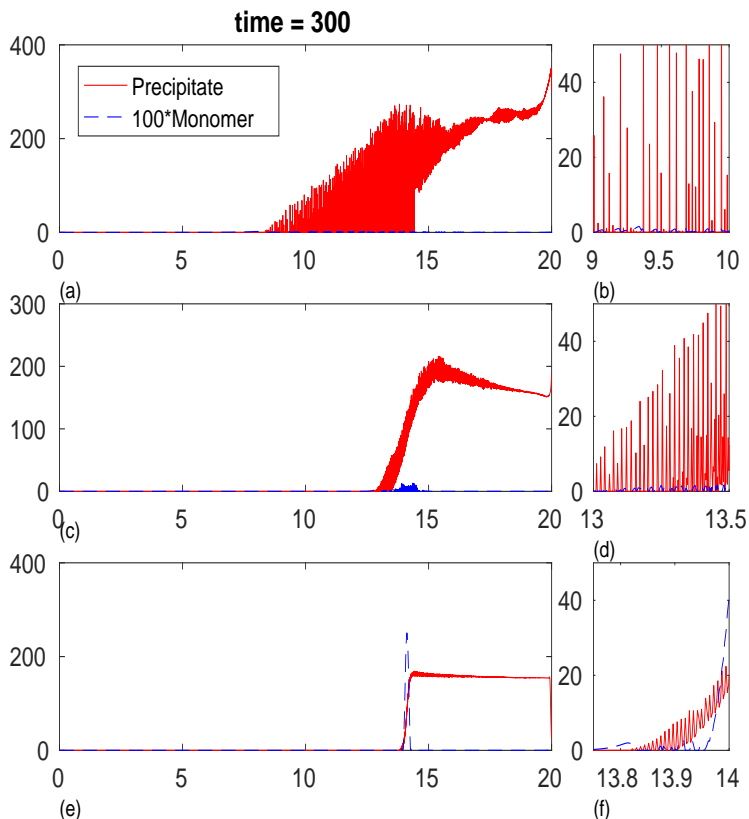
Figure 4.6: Numerical Simulation: At $t = 300$ precipitate in tube with $a_0 = a_1 = 77$, $b_0 = 45$, $b_1 = 0$ $\kappa = 2$, $\phi = 0.998$, $\gamma = 0.018$ and $\eta = 20000$. (a) Precipitate formation with $k = 0.01$ (b) Magnification of (a) from $x = 9 - 10$ (c) Precipitate formation with $k = 1$ (d) Magnification of (c) from $x = 13 - 13.5$ (e) Precipitate formation with $k = 100$ (f) Magnification of (e) from $x = 13.7 - 14$.
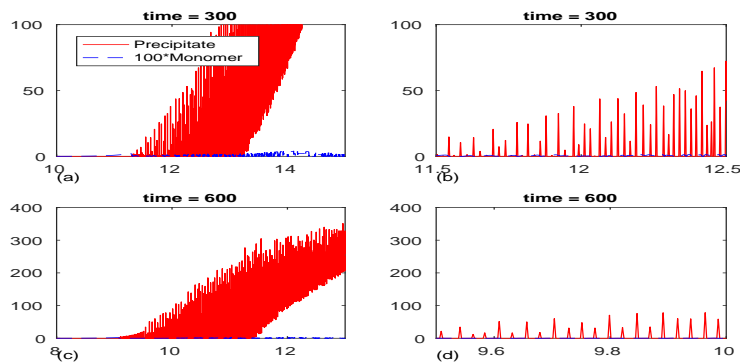
Figure 4.7: Numerical Simulation: Precipitate in tube with $a_0 = a_1 = 77$, $b_0 = 45$, $b_1 = 0$, $k = 0.01$, $\kappa = 2$, $\phi = 0.998$, $\gamma = 0.018$ and $\eta = 20000$. (a) Precipitate formation at the reaction front at 300 seconds (b) Close up of tail end of reaction front at 300 seconds (c) Precipitate formation at the reaction front at 600 seconds (b) Close up of tail end of reaction front at 600 seconds.

32
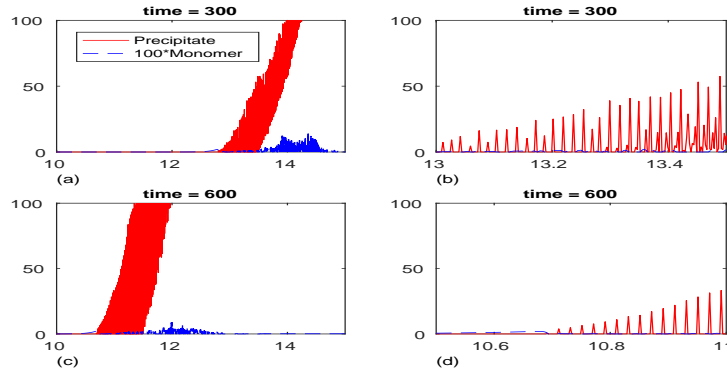
Figure 4.8: Numerical Simulation: Precipitate in tube with $a_0 = a_1 = 77$, $b_0 = 45$, $b_1 = 0$, $k = 1$, $\kappa = 2$, $\phi = 0.998$, $\gamma = 0.018$ and $\eta = 20000$. (a) Precipitate formation at the reaction front at 300 seconds (b) Close up of tail end of reaction front at 300 seconds (c) Precipitate formation at the reaction front at 600 seconds (b) Close up of tail end of reaction front at 600 seconds.
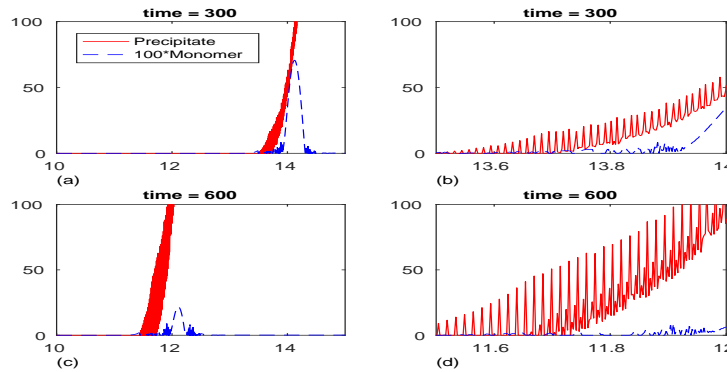
Figure 4.9: Numerical Simulation: Precipitate in tube with $a_0 = a_1 = 77$, $b_0 = 45$, $b_1 = 0$, $k = 10$, $\kappa = 2$, $\phi = 0.998$, $\gamma = 0.018$ and $\eta = 20000$. (a) Precipitate formation at the reaction front at 300 seconds (b) Close up of tail end of reaction front at 300 seconds (c) Precipitate formation at the reaction front at 600 seconds (b) Close up of tail end of reaction front at 600 seconds.
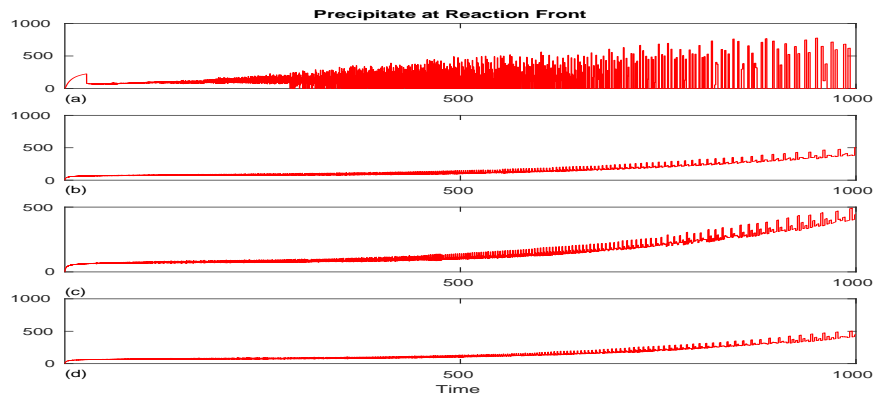
Figure 4.10: Simulation amplitude at reaction front with (a) $k = 0.01$ (b) $k = 3$ (c) $k = 5$ (d) $k = 7$.
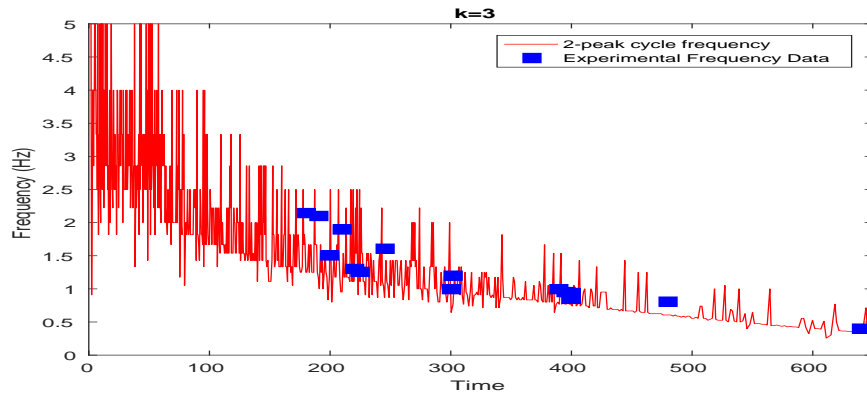
Figure 4.11: Simulation precipitate formation frequency at reaction front from $t = 0 - 1000$ with $k = 3$.
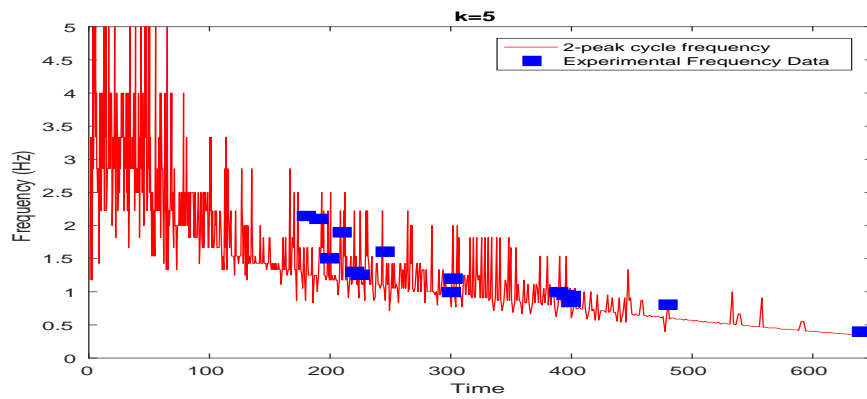
Figure 4.12: Simulation precipitate formation frequency at reaction front from $t = 0 - 1000$ with $k = 5$.
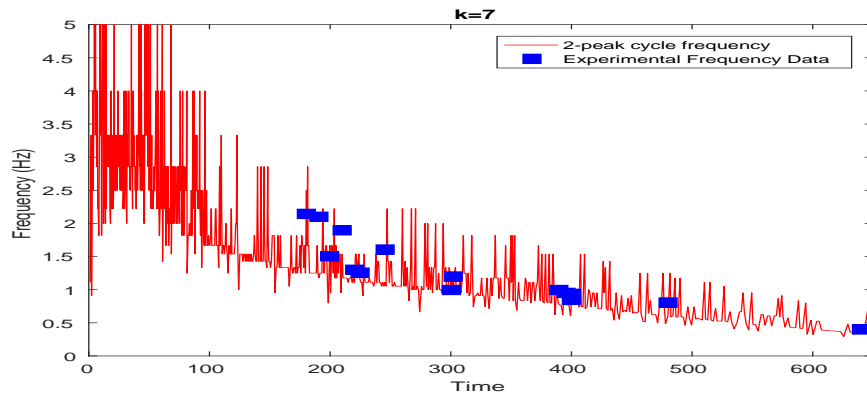
Figure 4.13: Simulation precipitate formation frequency at reaction front from $t = 0 - 1000$ with $k = 7$.

amplitude data provided in [1] is based on the relative brightness of pixel data so there is no quantitative method to compare the amplitude data with our simulations. However, we can analyze it qualitatively. Since rings are not observed in the actual experiment, we believe that $k \geq 1$. In Fig. 4.10, we have the amplitude plot for $k = [0.01, 3, 5, 7]$. In all cases, we can increase in the amplitude of the precipitary oscillations with time.

The second claim in [1] is the decrease in the oscillation's frequency with time. In Fig. 4.11, we plot the experimental frequency along with simulation frequency at $k = 3$. Qualitatively we can demonstrate that the oscillation's frequency decreases with time. We also believe that we quantitatively match the data within a small enough error. As we increase the reaction rate to $k = 5, 7$, in Figs. 4.12-4.13 we can see that within an error, our simulations match experimental data in [1]. In Section 4.2, we present simulation results in a two-dimensional domain.

4.2   Two-Dimensional Simulations

Similar to the one-dimensional simulations in the previous section, we have conducted two-dimensional simulations based on the experiments in [1]. As discussed previously, the reaction rate k is the most important parameter in our system and was varied in multiple simulations. Unlike the case in one-dimensional simulations, the two-dimensional simulation reveal underlying bifurcating patterns based on varying the reaction rate k that was not visible in the one dimensional simulations. In this section, we will first present the two-dimensional simulations with varying values of the reaction rate. We will discuss the patterns that form and provide an explanation on the apparent discrepancy between one-dimensional and two-dimensional simulations.

In Fig. 4.14-4.15, we present the results of our two-dimensional simulations for varying values of the reaction rate k. All other parameter values are consistent with the experiments conducted in [1]. In these saturated-vapor simulations, the tube is flooded with hydrogen chloride and ammonia vapor is introduced from the right hand of the figure.

In Fig. 4.14, $k = 0.01$. As the reaction front moves from right to left of the 20 cm reaction tube, we can see distinct rings form as time progresses. The results in Fig. 4.14(a)-(b) are surprising for

35

a multiple of reasons: (1) The structure for Liesegang rings forms very early in the reactions, (2) Liesegang rings form in consistency with spacing and time laws and (3) Precipitate is present in between the clearly defined rings.

In Fig. 4.14, $k = 1$. Although Liesegang rings do not appear to obey the spacing and time laws as in Fig. 4.15, we can see the formation of rings that are spatially more uniform. This is consistent with the one-dimensional simulations as described in Fig. 4.7.

With a different domain size in Fig. 4.16, the *tube* is inundated with hydrogen chloride at 77 mm/Hg and ammonia is introduced at the top at 45 mm/Hg. As a result a reaction front of ammonium chloride is formed that forms precipitate as it moves down the tube. Visually, rings can be seen $2 - 3$ cm down the tube with uniform precipitate before it. It is our belief that with a fine enough mesh, precipitary oscillations can be seen visually, but may already exist numerically. A close up of the area of Liesegang ring formation is provided in Fig. 4.17.

By changing the topological structure of the boundary source, we can also develop curved rings as illustrated in Fig. 4.18. We can now simulate experiments described in [6]. However, this is beyond the scope of this thesis.

Precipitate t=100
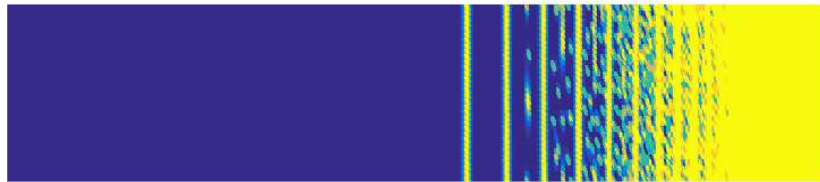
(a)

Precipitate t=300
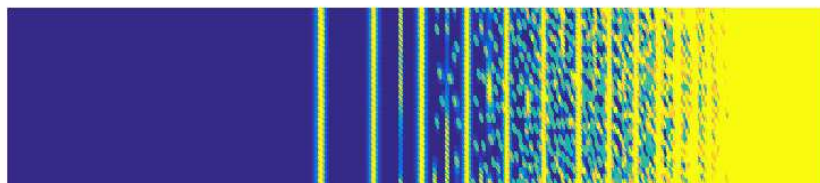
(b)

Figure 4.14: Numerical Simulation: Reaction front and precipitate formation at $t = 10$ and $t = 100$ with $a_0 = a_1 = 77mm/Hg$, $b_0 = 45mm/Hg$, $b_1 = 0$, $k = 0.01$, $\kappa = 2$, $\phi = 0.998$, $\gamma = 0.018$ and $\eta = 20000$.
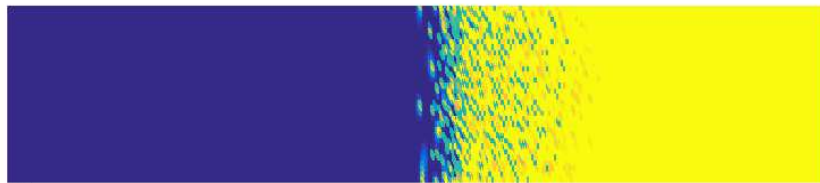
Figure 4.15: Numerical Simulation: Reaction front and precipitate formation at $t = 10$ and $t = 100$ with $a_0 = a_1 = 77mm/Hg$, $b_0 = 45mm/Hg$, $b_1 = 0$, $k = 1$, $\kappa = 2$, $\phi = 0.998$, $\gamma = 0.018$ and $\eta = 20000$.
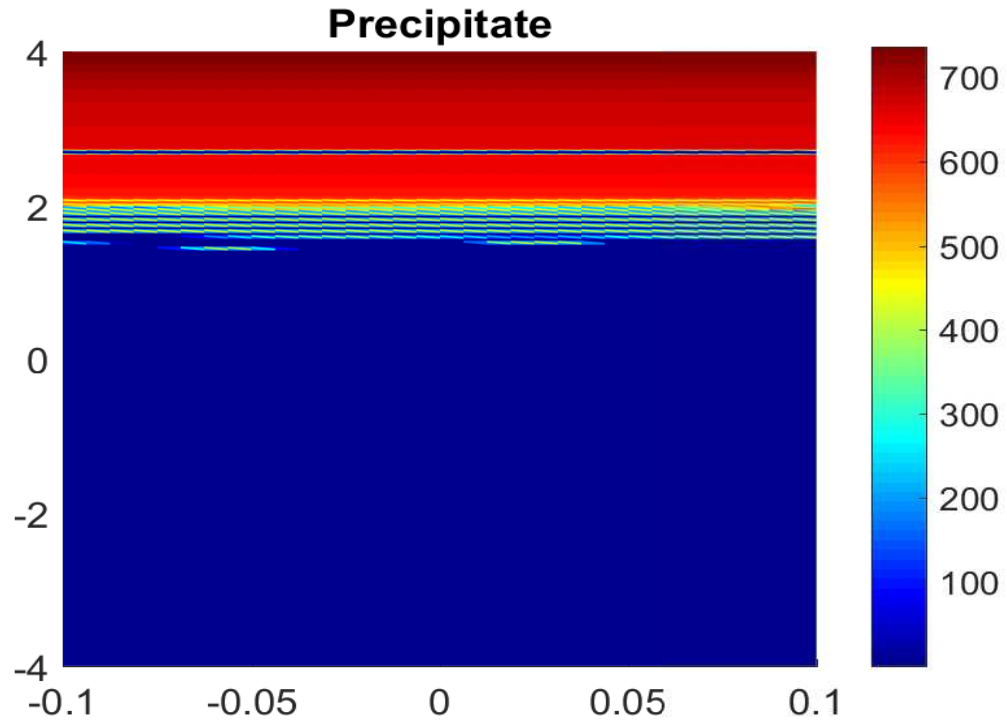
Figure 4.16: Numerical Simulation: Precipitate in tube with $a_0 = a_1 = 77$, $b_0 = 45$, $b_1 = 0$, $k = 0.1$, $\kappa = 2$, $\phi = 0.98$, $\gamma = 0.018$ and $\eta = 10000$.
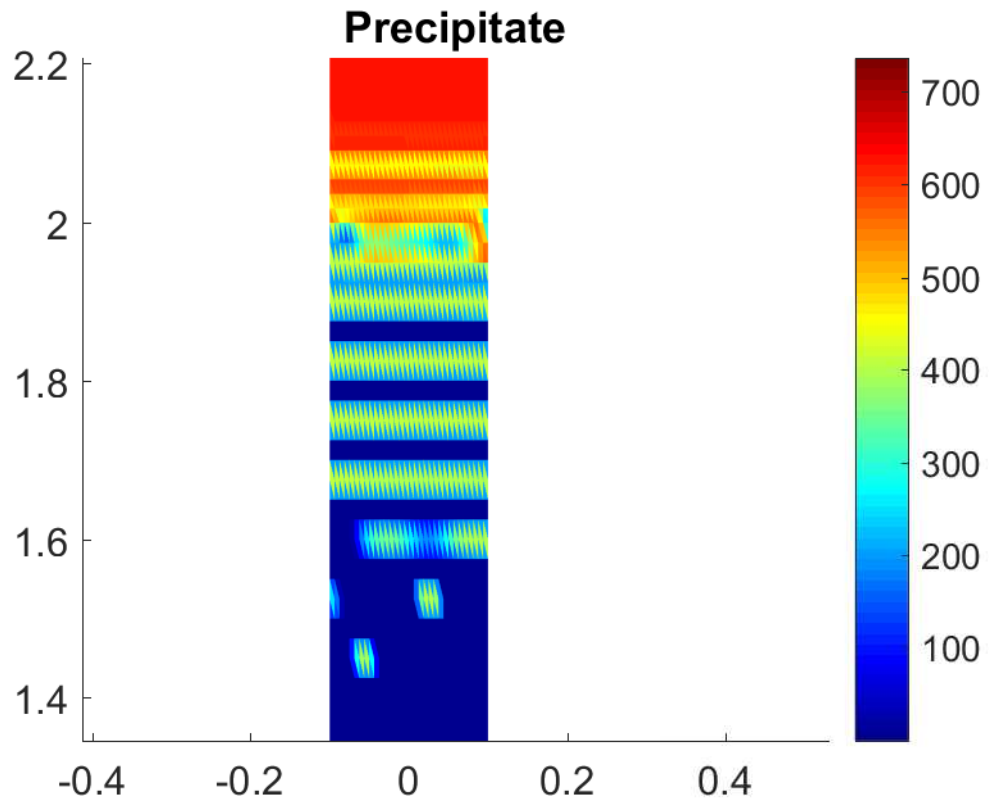
Figure 4.17: A zoom in of the precipitate bands in Fig. 4.16
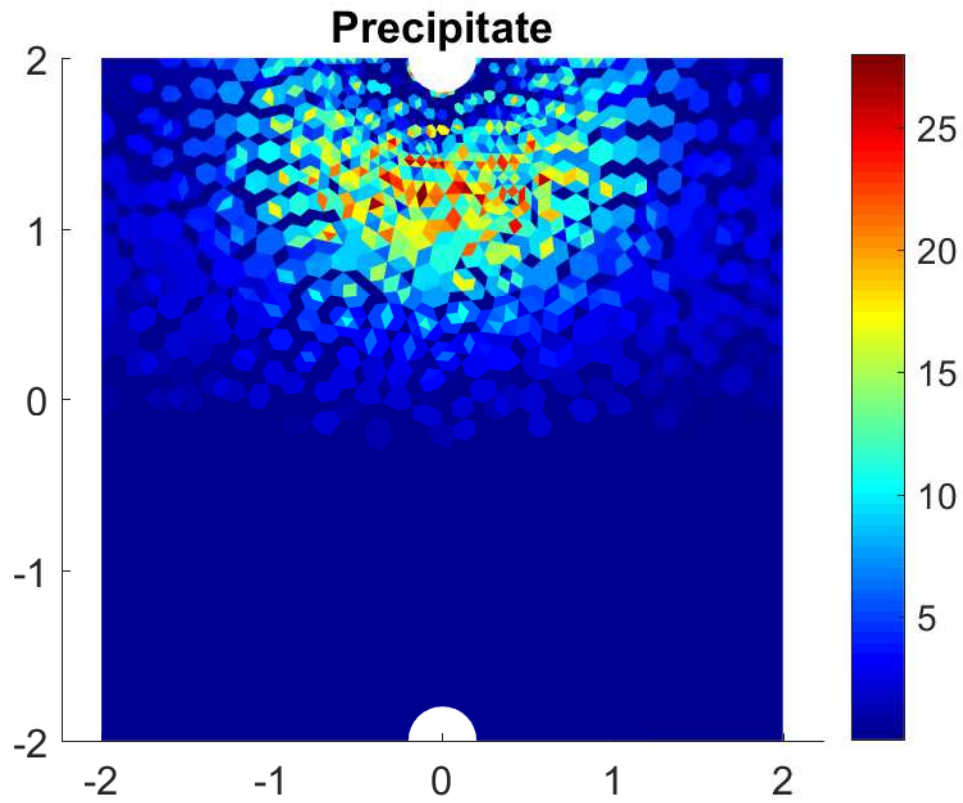
Figure 4.18: Numerical Simulation: Precipitate in petri dish with reactants source introduces as circular droplet. $a_0 = 10$, $a_1 = 0$, $b_0 = 2$, $b_1 = 0$, $k = 0.1$, $\kappa = 2$, $\phi = 0.998$, $\gamma = 0.018$ and $\eta = 20000$.

Chapter 5

Square Arrays in Ion Bombardment of a Binary Crystalline Material

The work in most of this chapter has been published[5]. The paper published is presented in Section 5.1-5.6.

5.1 Introduction

When the planar surface of a binary material is bombarded with a broad ion beam, generally one of the two atomic species is preferentially sputtered, and, as a consequence, a surface layer of altered composition develops. If the solid surface is not flat initially, the spatial variation of the surface height can lead to a surface composition that varies from point to point. This spatially varying surface composition in turn influences the time evolution of the surface topography [20]. The dynamics of the surface morphology and composition are therefore coupled.

This coupling can lead to intriguing types of pattern formation and to a higher degree of order than can be achieved if a surface layer of altered composition is not present. Normal-incidence bombardment of GaSb, for example, can produce an array of nanodots with a remarkable degree of hexagonal order [21–24]. In the case of oblique-incidence bombardment, nearly defect free surface ripples may develop with a spatially oscillating surface composition that mirrors the oscillations of the surface height [25–27]. A "dots-on-ripples" topography in which dots that form a hexagonal array sit atop a ripple topography can also emerge as a result of the coupling [26].

In the models that have been developed so far for these phenomena, it is assumed that the solid is either amorphous or that a surface layer is amorphized by the impinging ions. This assumption is valid, for example, if the target material is a semiconductor that is maintained at a temperature

---

below its recrystallization temperature T_R. However, if the target is a metal single crystal, the crystal structure is not significantly disrupted by the ion bombardment. This is also the case if the target is a crystalline semiconductor held at a temperature T in excess of T_R.

Pattern formation on the surface of elemental materials that remain crystalline during ion bombardment is strongly influenced by the Ehrlich-Schwoebel (ES) barrier [28–31]. The ES barrier produces an uphill atomic current on the crystal's surface and so tends to destabilize an initially flat surface. This current is typically anisotropic, which is a manifestation of the anisotropy of the underlying crystal lattice.

When an Ag (001) surface at a temperature of 200 K was bombarded at normal incidence with a 1 keV Ne^+ beam, a disordered checkerboard pattern of inverted four-sided pyramids was observed [32]. Analogous patterns formed when the (001) surface of germanium was bombarded at normal incidence and T was maintained at a value not too far in excess of T_R [33]. In both of these experiments, the patterns formed were disordered and there was no surface layer of altered composition. These observations suggest a question: Can highly ordered square arrays of nanoscale pyramids or pyramidal pits be produced by normal-incidence bombardment of the (001) surface of a crystalline binary material?

In this paper, we will study the nanoscale patterns formed when the (001) surface of a crystalline binary material with fourfold rotational symmetry about the z axis is subjected to normal-incidence ion bombardment. We will assume that the material's crystal structure is left intact by the impinging ions; this is a reasonable assumption if the material is a substitutional alloy of two metals or if it is a binary semiconductor that is held at a temperature above T_R. As we will demonstrate, for certain ranges of the parameters, highly ordered square arrays of four-sided pyramids emerge. An Ehrlich-Schwoebel barrier is essential if patterns of this kind are to form — diffusional anisotropy alone does not yield orderly square arrays.

This paper is organized as follows: We develop the equations of motion in Section 5.2. In Section 5.3, we find the domain in parameter space in which there is a narrow band of unstable wavelengths. It is in this region of parameter space that a Turing instability that leads to a well-

ordered pattern may occur. In Section 5.4, we derive the amplitude equations which describe the pattern formation that occurs near the Turing instability. Stability analysis of the steady-state solutions to the amplitude equations gives rise to conditions for the formation of ripple or square patterns. In Section 5.5, we carry out numerical simulations of the original equations of motion developed in Section 5.2 and compare the results with the amplitude equation analysis. Physical implications of our results and a summary of our conclusions are given in Section 5.6.

5.2   Equations of Motion

In groundbreaking work, Shenoy, Chan and Chason studied the coupling between the surface topography and composition that arises during ion bombardment of a binary compound [20]. Bradley and Shipman (BS) extended this theory to include the effect of mass redistribution and the leading order nonlinear terms [22–24]. The BS equations govern the behavior of $u(x, y, t)$ and $\phi(x, y, t)$, the deviations of the surface height and surface concentration from their unperturbed, steady-state values. Using the same notation, assumptions and rescaling as BS employed, we have

$$\frac{\partial u}{\partial t} = \phi - \nabla^2 u - \nabla^2 \nabla^2 u + \lambda (\nabla u)^2 \tag{5.1}$$

and

$$\frac{\partial \phi}{\partial t} = -a\phi + b\nabla^2 u + c\nabla^2 \phi + \nu \phi^2 + \eta \phi^3 \tag{5.2}$$

for normal-incidence bombardment. Explicit expressions that relate the dimensionless constants a, b, c, λ, ν and η to the underlying physical parameters may be found in Ref. [23].

It is assumed that the binary solid is either amorphous or that the incident ions amorphize a layer at the surface of the solid in the BS theory. The surface mass currents included in the theory result from surface diffusion and ion-induced mass redistribution.

In this paper, we will study the time evolution of the (001) surface of a crystalline binary solid that is bombarded with a broad ion beam at normal incidence. We assume that the crystal structure of the solid has fourfold rotational symmetry about the z axis. Examples of binary compound

44

semiconductors having this property are the IV-VI materials PbSe, PbS, PbTe and SnTe, all of which have the halite crystal structure.

When the semiconducting compounds GaAs and InAs are subjected to normal-incidence bombardment at temperatures in excess of T_R, nearly defect free surface ripples result [34]. These materials have a zincblende crystal structure. As a result, they only have twofold rotational symmetry about the z axis. The theory developed here therefore does not apply to these experiments.

Although the incident ions introduce defects into the crystal lattice, it will be assumed that these are rapidly annealed away so that the solid remains a nearly defect-free crystal during the bombardment. In this case, the ES surface atomic currents must be added to the currents that stem from surface diffusion and mass redistribution. The surface currents of the two atomic species A and B that are produced by the ES barrier may be written [29, 31]

$$\boldsymbol{J}_i^{(\text{ES})} = e_i u_x (1 - p_i u_x^2 - q_i u_y^2) u_y (1 - q_i u_x^2 - p_i u_y^2)). \tag{5.3}$$

Here $i = A$, B, the subscripts on u denote partial derivatives and e_A, e_B, p_A, p_B, q_A and q_B are constants that depend on the choice of target material and ion beam. In addition, surface diffusion is in general anisotropic on the crystal surface. In the BS theory, the surface currents produced by surface diffusion and capillarity are isotropic and may be written

$$\boldsymbol{J}_i^{(\text{SD})} = D_i \boldsymbol{\nabla} \nabla^2 u, \tag{5.4}$$

where $i = A$, B and the positive constants D_A and D_B are proportional to the diffusivities of the two atomic species. These currents take the form

$$\boldsymbol{J}_i^{(\text{SD})} = D_i \boldsymbol{\nabla} \nabla^2 u + C_i (u_{xyy} \hat{\boldsymbol{x}} + u_{xxy} \hat{\boldsymbol{y}}) \tag{5.5}$$

for the problem at hand. The magnitudes of the constants C_A and C_B gauge the extent to which the surface diffusion is anisotropic on the crystal's surface. In the BS theory, $e_A = e_B = C_A = C_B = 0$.

We now adopt the same assumptions and approximations as BS employed, except that it will be assumed that the solid remains crystalline during the ion bombardment, as we already stated. The analysis very closely parallels the detailed derivation in Ref. [23] and so we will only give the resulting rescaled equations of motion. They are

$$u_t = \phi - \nabla^2 u - \nabla^2 \nabla^2 u + \lambda (\nabla u)^2 + \rho u_{xxyy} + \partial_x [u_x (\alpha_1 u_x^2 + \beta_1 u_y^2)] + \partial_y [u_y (\beta_1 u_x^2 + \alpha_1 u_y^2)] \quad (5.6)$$

and

$$\phi_t = -a\phi + b\nabla^2 u + c\nabla^2 \phi + \nu \phi^2 + \eta \phi^3 + \partial_x [u_x (\alpha_2 u_x^2 + \beta_2 u_y^2)] + \partial_y [u_y (\beta_2 u_x^2 + \alpha_2 u_y^2)]. \quad (5.7)$$

The explicit expressions that relate the dimensionless parameters a, b, c, λ, ν, η, ρ, α_1, α_2, β_1 and β_2 to the underlying physical parameters are readily obtained. They are, however, quite lengthy and not particularly illuminating and so we will not pause to list them here. If there is no ES barrier, then $\alpha_1 = \alpha_2 = \beta_1 = \beta_2 = 0$ and if, in addition, diffusion is isotropic, then $\rho = 0$. In that event, the BS equations (5.1) and (5.2) are recovered.

If the term ϕ is dropped from Eq. (5.6), the surface morphology is not coupled to the composition. The resulting equation is similar to the equation of motion used by Ou *et al.* to model normal-incidence bombardment of the (001) surface of a germanium sample held at a temperature above its recrystallization temperature [33]. In the model employed by Ou *et al.*, however, $\rho = \lambda = \beta_1 = 0$. This means that they assumed the surface diffusion to be isotropic, neglected the nonlinearity coming from sputtering, and adopted a particular form for the ES terms. These simplifications seem to be good approximations for their experiments. Ou *et al.* also included the conserved Kuramoto-Sivashinsky nonlinearity $\nabla^2 (\nabla u)^2$ in their equation of motion. This leads the surface patterns to coarsen with time, in accord with their experiments.

In our model, it is sufficient to consider only values of the parameter ρ that are less than or equal to zero. To see this, we choose a new coordinate system that is obtained by rotating the original coordinate system by $45°$ and then rescaling [35]. Explicitly, we set $\tilde{x} = (2r)^{-1/2}(x + y)$, $\tilde{y} = (2r)^{-1/2}(-x + y)$, $\tilde{t} = r^{-1}t$, $\tilde{u} = u$ and $\tilde{\phi} = r\phi$, where $r \equiv 1 - \rho/4$. This yields

$$\tilde{u}_{\tilde{t}} = \tilde{\phi} - \tilde{\nabla}^2\tilde{u} - \tilde{\nabla}^2\tilde{\nabla}^2\tilde{u} + \tilde{\lambda}(\tilde{\nabla}u)^2 + \tilde{\rho}\tilde{u}_{\tilde{x}\tilde{x}\tilde{y}\tilde{y}} + \partial_{\tilde{x}}[\tilde{u}_{\tilde{x}}(\tilde{\alpha}_1\tilde{u}_{\tilde{x}}^2 + \tilde{\beta}_1\tilde{u}_{\tilde{y}}^2)] + \partial_{\tilde{y}}[\tilde{u}_{\tilde{y}}(\tilde{\beta}_1\tilde{u}_{\tilde{x}}^2 + \tilde{\alpha}_1\tilde{u}_{\tilde{y}}^2)] \quad (5.8)$$

and

$$\tilde{\phi}_{\tilde{t}} = -\tilde{a}\tilde{\phi} + \tilde{b}\tilde{\nabla}^2\tilde{u} + \tilde{c}\tilde{\nabla}^2\tilde{\phi} + \tilde{\nu}\tilde{\phi}^2 + \tilde{\eta}\tilde{\phi}^3 + \partial_{\tilde{x}}[\tilde{u}_{\tilde{x}}(\tilde{\alpha}_2\tilde{u}_{\tilde{x}}^2 + \tilde{\beta}_2\tilde{u}_{\tilde{y}}^2)] + \partial_{\tilde{y}}[\tilde{u}_{\tilde{y}}(\tilde{\beta}_2\tilde{u}_{\tilde{x}}^2 + \tilde{\alpha}_2\tilde{u}_{\tilde{y}}^2)]. \quad (5.9)$$

Here $\tilde{a} = ra$, $\tilde{b} = rb$, $\tilde{c} = c$, $\tilde{\lambda} = \lambda$, $\tilde{\nu} = \nu$, $\tilde{\eta} = r^{-1}\eta$,

$$\tilde{\rho} = -\frac{\rho}{1 - \rho/4}, \quad (5.10)$$

$$\tilde{\alpha}_1 = \frac{1}{4r}(\alpha_1 + \beta_1), \quad (5.11)$$

$$\tilde{\beta}_1 = \frac{1}{4r}(3\alpha_1 - \beta_1), \quad (5.12)$$

$$\tilde{\alpha}_2 = \frac{1}{4}(\alpha_2 + \beta_2), \quad (5.13)$$

and

$$\tilde{\beta}_2 = \frac{1}{4}(3\alpha_2 - \beta_2). \quad (5.14)$$

If we were to drop the tildes, Eqs. (5.8) and (5.9) would be identical to Eqs. (5.6) and (5.7). We shall see in the next section that for the theory to be well posed, ρ must be less than 4. Thus, if ρ is positive, Eq. (5.10) shows that we may adopt a rotated and rescaled coordinate system in which $\tilde{\rho}$ (the transformed value of ρ) is negative. We will therefore confine our attention to $\rho \leq 0$ in what follows.

5.3   Linear Stability Analysis

We now determine whether or not the flat, compositionally homogeneous steady-state solution $u = \phi = 0$ is linearly stable for a given set of parameter values. Consider a perturbation to the steady state that is small enough that the nonlinear terms may be dropped from Eqs. (5.6) and (5.7), yielding the linearized equations of motion. We seek solutions to these equations of the form

$$u = u_* \exp(i\boldsymbol{k} \cdot \boldsymbol{x} + \sigma t), \;\; \phi = \phi_* \exp(i\boldsymbol{k} \cdot \boldsymbol{x} + \sigma t), \tag{5.15}$$

where $\boldsymbol{k} \equiv k_x \hat{x} + k_y \hat{y}$, $\boldsymbol{x} \equiv x\hat{x} + y\hat{y}$ and u_* and ϕ_* are constants. $\mathrm{Re}\,\sigma$ gives the rate with which the amplitude of the mode grows (for $\mathrm{Re}\,\sigma > 0$) or attenuates (for $\mathrm{Re}\,\sigma < 0$). For each wavevector $\boldsymbol{k}$, there are two possible values of σ, given by

$$2\sigma_\pm = f \pm \sqrt{g}, \tag{5.16}$$

where $k \equiv |\boldsymbol{k}|$,

$$f(k, a, c, \alpha) \equiv -a + (1 - c)k^2 - k^4 + \rho k_x^2 k_y^2 \tag{5.17}$$

and

$$g(k, a, b, c, \alpha) \equiv \left[a + (1 + c)k^2 - k^4 + \rho k_x^2 k_y^2 \right]^2 - 4bk^2. \tag{5.18}$$

We will assume that $\rho < 4$ since in that case $\mathrm{Re}\,\sigma_+$ and $\mathrm{Re}\,\sigma_-$ are both negative for sufficiently large wavenumbers k, and the theory is therefore well posed.

The remainder of the linear stability analysis closely parallels that given elsewhere [23] for the special case $\rho = 0$ and so only the results will be given. For fixed $\rho \leq 0$, we partition the positive quadrant of the (a, c) plane into three regions (see Figure 1 of Ref. [[23]]):

In Region I, $c > a$ and $4a > (1 - c)^2$ if $c < 1$;

In Region II, $c < a$ and $4a > (1 - c)^2$ if $c < 1$;

In Region III, $c < 1$ and $4a < (1 - c)^2$.

The necessary and sufficient condition for the solid surface to be unstable in Region I is $b < b_T$, where

$$b_T \equiv \frac{(c+a)^2}{4c}. \tag{5.19}$$

The surface is unstable in Region II if $b < a$. Finally, in Region III, the surface is unstable for arbitrary values of b.

For the weakly nonlinear analysis that follows, we will confine our attention to Region I since it is for parameter values in this region that stable well-ordered patterns can form. Consider the case $b = b_T$. If $\rho < 0$ and the point (a, c) lies in Region I, then σ_+ is zero for $\boldsymbol{k} = 0$ and $\pm \boldsymbol{k}_1$ and $\pm \boldsymbol{k}_2$, where $\boldsymbol{k}_1 \equiv k_T \hat{x}$, $\boldsymbol{k}_2 \equiv k_T \hat{y}$ and k_T is given by

$$k_T^2 = \frac{c-a}{2c}. \tag{5.20}$$

If $\rho = 0$, on the other hand, then σ_+ is zero for $\boldsymbol{k} = 0$ and $\boldsymbol{k}$ such that $|\boldsymbol{k}| = k_T$. The real part of $\sigma_+(\boldsymbol{k})$ is negative for all other $\boldsymbol{k}$ for both $\rho = 0$ and $\rho < 0$. A Turing instability therefore occurs for $b = b_T$ [36–38]. For b just below b_T, there is a narrow annular region in $\boldsymbol{k}$ space in which $\operatorname{Re} \sigma_+(\boldsymbol{k}) > 0$ for the case $\rho = 0$, whereas for $\rho < 0$, there are small regions in $\boldsymbol{k}$ space about each of the points $\pm \boldsymbol{k}_1$ and $\pm \boldsymbol{k}_2$ in which $\operatorname{Re} \sigma_+(\boldsymbol{k})$ is positive. These regions are shown in Fig. 5.1.

5.4   Weakly nonlinear analysis

We now analyze Eqs. (5.6) and (5.7) close to the Turing transition. We assume that the values of the parameters a and c lie in Region I so that $c > a$ and $4a > (1 - c)^2$ if $c < 1$. The bifurcation parameter b is taken to be slightly below the critical value b_T: we set $b = b_T - \epsilon$, where $\epsilon > 0$ is small and positive. As discussed in Sec. 5.3, if $\rho < 0$ and b is close enough to b_T, then there are small regions about the wavevectors $\pm \boldsymbol{k}_1$ and $\pm \boldsymbol{k}_2$ in which $\operatorname{Re} \sigma_+(\boldsymbol{k})$, is positive; if $\rho = 0$, there is an annular region of such modes. The analysis, which yields ordinary differential equations for the time-evolution of the amplitudes of these unstable modes [36–38], is similar to that we have
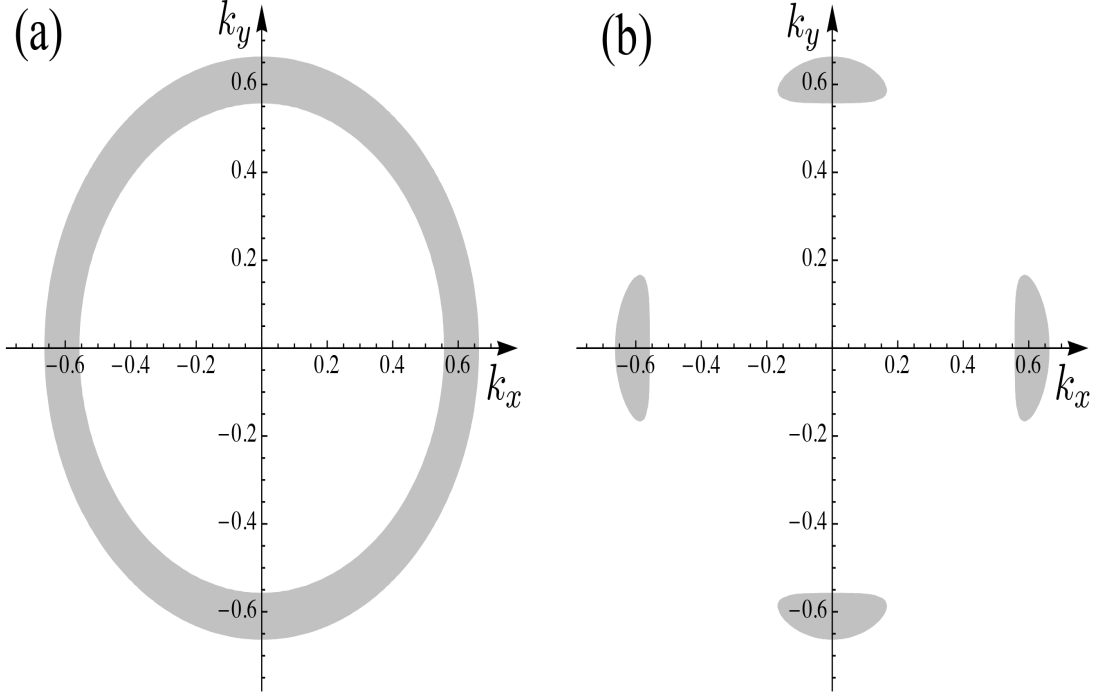
Figure 5.1: Regions in wavevector space in which $\mathrm{Re}\,\sigma_+(\boldsymbol{k}) > 0$ for $a = 0.25$ and $c = 1$ (shaded). In (a) $\rho = 0$ and $b = 0.99b_T \simeq 0.3867$, while in (b) $\rho = -0.25$ and $b = 0.99b_T \simeq 0.3867$.

given elsewhere [22, 23] for normal-incidence ion bombardment of binary materials and so only the principal results will be given here.

We obtain approximate solutions to the equations of motion of the form

$$\begin{pmatrix} u \\ \phi \end{pmatrix} = \sum_{j=1}^{2} \begin{pmatrix} 1 \\ \frac{a^2 - c^2}{4c^2} \end{pmatrix} (A_j e^{i\boldsymbol{k}_j \cdot \boldsymbol{x}} + \mathrm{c.c.}) + \begin{pmatrix} G \\ 0 \end{pmatrix}, \tag{5.21}$$

where the complex-valued amplitudes A_j and real-valued amplitude G vary slowly with time and c.c. denotes the complex conjugate. The Goldstone mode with $u = G$ and $\phi = 0$ corresponds to the neutrally stable wavenumber $k = 0$; physically, this mode is simply a vertical displacement of the surface. Although this mode is not linearly unstable, it may not be neglected, due to its interactions with the linearly unstable modes through the nonlinear terms in the equations of motion. In the case $\rho < 0$, the vectors $\boldsymbol{k}_j$ in the sum in Eq. (5.21) are $\boldsymbol{k}_1 = k_T \hat{x}$ and $\boldsymbol{k}_2 = k_T \hat{y}$ since the corresponding

50

Fourier modes have the largest growth rates. In the case in which ρ vanishes, $\boldsymbol{k}_1$ and $\boldsymbol{k}_2$ could be any pair of vectors with length k_T.

The solvability conditions obtained by expanding Eqs. (5.6) and (5.7) to second order in ϵ yield equations that govern the time dependence of the amplitudes A_1, A_2 and G. We find that

$$\frac{dA_1}{dt} = \sigma A_1 - \gamma A_1(\gamma_1|A_1|^2 + \gamma_2|A_2|^2), \tag{5.22}$$

$$\frac{dA_2}{dt} = \sigma A_2 - \gamma A_2(\gamma_2|A_1|^2 + \gamma_1|A_2|^2), \tag{5.23}$$

where

$$\sigma \equiv \frac{2c(c-a)}{(c+a)(2c^2+a-c)}(b_T - b), \tag{5.24}$$

$$\gamma \equiv \frac{2c^2}{2c^2+a-c}, \tag{5.25}$$

and in the case $\rho < 0$,

$$\gamma_1 \equiv \frac{3\eta(c-a)^3(a+c)^2}{32c^6} + 3(a\alpha_1 + c\alpha_1 + 2\alpha_2), \tag{5.26}$$

and

$$\gamma_2 \equiv \frac{6\eta(c-a)^3(a+c)^2}{32c^6} + 4(a\beta_1 + c\beta_1 + 2\beta_2). \tag{5.27}$$

If $\rho = 0$, the coefficients of the cubic terms in Eqs. (5.22) and (5.23) are functions of the wavevectors $\boldsymbol{k}_1$ and $\boldsymbol{k}_2$. Setting $c_j = \cos(\theta_j)$, $s_j = \sin(\theta_j)$, and $\boldsymbol{k}_j = k_T(c_j, s_j)$ for $j = 1$ and 2, the coefficients γ_1 and γ_2 become

$$\gamma_1 \equiv \frac{3\eta(c-a)^3(a+c)^2}{32c^6} + 3(a\alpha_1 + c\alpha_1 + 2\alpha_2)(c_1^4 + s_1^4) + 6(a\beta_1 + c\beta_1 + 2\beta_2)c_1^2 s_1^2, \tag{5.28}$$

and

$$\gamma_2 \equiv \frac{6\eta(c-a)^3(a+c)^2}{32c^6} + 6(a\alpha_1 + c\alpha_1 + 2\alpha_2)(c_1^2 c_2^2 + s_1^2 s_2^2) + 4(a\beta_1 + c\beta_1 + 2\beta_2)(c_1^2 s_2^2 + c_1 s_1 c_2 s_2 + s_1^2 c_2^2).$$

(5.29)

We also obtain

$$\frac{dG}{dt} = \left[\lambda \left(1 - \frac{a}{c} \right) + \frac{2\nu}{a} \left(\frac{c^2 - a^2}{4c^2} \right)^2 \right] (|A_1|^2 + |A_2|^2)$$

(5.30)

for any value of ρ. The value of dG/dt gives the change in the net sputter yield that stems from the spatial variations in the surface height and composition. As shown by Eq. (5.30), dG/dt may be either positive or negative, depending on the values of the coefficients. Thus, the Goldstone mode either increases the spatially-averaged sputter yield (if $dG/dt < 0$) or reduces it (if $dG/dt > 0$). The real amplitude G does not appear on the right-hand side of either Eqs. (5.22), (5.23) or (5.30) since only derivatives of u appear in the equations of motion, and we are assuming that G does not vary in space.

A detailed analysis of the amplitude equations (5.22) and (5.23) may be found in Ref. [[36]]; here we summarize the results. The system of equations (5.22) and (5.23) admits stationary solutions of three different types that are stable for some range of σ:

1. *Homogeneous state:* $A_1 = A_2 = 0$. This solution is the undisturbed steady state $u = \phi = 0$ and is stable for $\sigma < 0$ (equivalently, for $b > b_T$).

2. *Roll pattern:* $A_1 = (\sigma/\gamma\gamma_1)^{1/2}e^{ip}$ and $A_2 = 0$, or $A_1 = 0$ and $A_2 = (\sigma/\gamma\gamma_1)^{1/2}e^{ip}$. Here p is an arbitrary phase. These solutions are surface ripples (or "rolls") with wavevectors k_1 and k_2 and are stable for $\sigma > 0$ and $\gamma_1 < |\gamma_2|$.

3. *Square pattern:* $A_1^2 = \frac{\sigma}{\gamma(\gamma_1+\gamma_2)}e^{ip_1}$ and $A_2^2 = \frac{\sigma}{\gamma(\gamma_1+\gamma_2)}e^{ip_2}$, where p_1 and p_2 are arbitrary phases. These solutions are square arrays of nanodots or nanoholes and are stable for $\sigma > 0$ and $\gamma_1 > |\gamma_2|$.

If b is slightly less than b_T, then σ is positive and the flat steady-state solution is unstable. If $\rho < 0$ and $\gamma_1 < |\gamma_2|$, then partially intersecting patches of surface ripples with wavevectors k_1 and

52

$\mathbf{k}_2$ begin to form as the instability sets in. If, as in our idealized model, there is no source of noise, ultimately only one ripple orientation will survive and the fourfold rotational symmetry about the z axis will be broken. In an experiment, however, there is shot noise in the ion beam and one ripple orientation will never cover the entire sample.

For $\rho < 0$ and $\sigma > 0$, the condition $\gamma_1 > |\gamma_2|$ that must be satisfied for square solutions to be stable may be written

$$3(a+c)\alpha_1 + 6\alpha_2 > 3\xi(a+c) + 4(a+c)\beta_1 + 8\beta_2 \quad \text{if} \quad \gamma_2 > 0, \quad \text{or}$$

$$3(a+c)\alpha_1 + 6\alpha_2 > -9\xi(a+c) - 4(a+c)\beta_1 - 8\beta_2 \quad \text{if} \quad \gamma_2 < 0, \tag{5.31}$$

where $\xi \equiv \eta(c-a)^3(a+c)/(32c^6)$ is positive for a and c in Region I. For the simpler case in which $\alpha_2 = \beta_2 = 0$, this condition reduces to

$$\alpha_1 > \frac{4}{3}\beta_1 + \xi \quad \text{if} \quad \beta_1 > -\frac{2}{3}\xi, \quad \text{or}$$

$$\alpha_1 > -\frac{4}{3}\beta_1 - 3\xi \quad \text{if} \quad \beta_1 < -\frac{2}{3}\xi.$$

The region in the (α_1, β_1) plane for which square solutions are stable if $\alpha_2 = \beta_2 = 0$ is shown as the shaded region in Fig. 5.2. This region is bounded away from the origin in the (α_1, β_1) plane. In particular, if there is no Ehrlich-Schwoebel barrier (so that $\alpha_1 = \alpha_2 = \beta_1 = \beta_2 = 0$), a square array of nanodots or nanoholes is not stable. This means that diffusional anisotropy alone is not sufficient to stabilize a square pattern — an ES barrier is needed as well. Moreover, not just any ES terms will do — the ES coefficients must satisfy the condition (5.31) if a square pattern is to form.

Because $c > a$ in Region I, Eq. (5.21) shows that the spatial variations of u and ϕ are $180°$ out of phase. As a consequence, the preferentially sputtered species is most concentrated at the highest points of the surface.

53
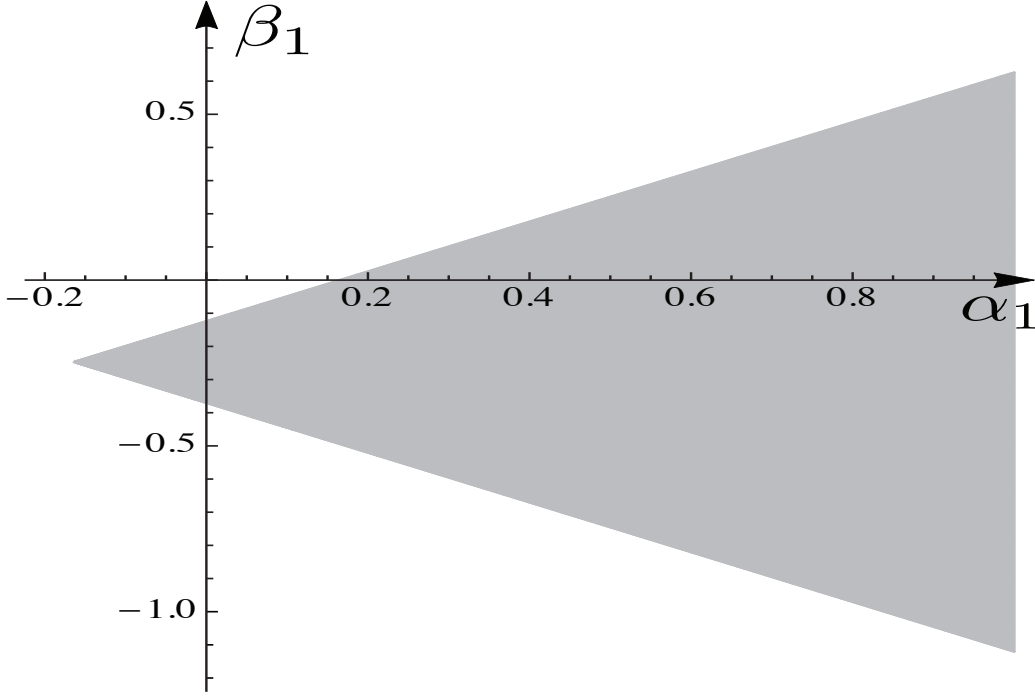
Figure 5.2: The region in the (α_1, β_1) plane for which $\gamma_1 > |\gamma_2|$ if $\alpha_2 = \beta_2 = 0$ is shaded. The other parameters are $a = 0.25$, $c = 1$, and $\eta = 10$. Square patterns are stable for (α_1, β_1) in this region if $\sigma > 0$.

The situation is completely analogous for $0 < \rho < 4$. The only difference between this case and the case $\rho < 0$ is that the two possible ripple wavevectors are $\boldsymbol{k}_3$ and $\boldsymbol{k}_4$, where $\boldsymbol{k}_3 \equiv k_T(\hat{x} + \hat{y})/\sqrt{2}$ and $\boldsymbol{k}_4 \equiv k_T(\hat{x} - \hat{y})/\sqrt{2}$ and k_T is given by

$$k_T^2 = \frac{c - (1 + \alpha)a}{2c(1 + \alpha)}. \tag{5.32}$$

As a consequence, the ripples form $45°$ angles with the $x-$ and $y-$axes when $\rho > 0$.

For the case $\rho = 0$, the linear stability analysis yields an entire annulus of wavevectors corresponding to unstable modes and therefore does not put any restriction on the angles θ_j. In fact, the wavevectors chosen by the dynamics may not even be orthogonal to each other. A prediction of the chosen angles θ_1 and θ_2 may be obtained by realizing that, although the system of partial differential equations (PDEs) given by Eqs. (5.8) and (5.9) is not a gradient system, the system of amplitude equations given by Eqs. (5.22) and (5.23) is. Indeed, defining the effective potential

$$P(A_1, A_1^*, A_2, A_2^*; \theta_1, \theta_2, \boldsymbol{p}) \equiv -\sigma(A_1 A_1^* + A_2 A_2^*) + \frac{1}{2}\gamma \left[\gamma_1 A_1^2 (A_1^*)^2 + 2\gamma_2 A_1 A_1^* A_2 A_2^* + \gamma_1 A_2^2 (A_2^*)^2 \right],$$

$$(5.33)$$

where $\boldsymbol{p}$ is the vector of parameters, the amplitude equations may be written as

$$\frac{dA_j}{dt} = -\frac{\partial}{\partial A_j^*} P$$

for $j = 1, 2$. This implies that the effective potential P decreases with time until a local minimum is reached and the pattern stops evolving.

For a given choice of the angles θ_j, the system of amplitude equations may be solved for the stationary pattern $A_1^2 = A_2^2 = \frac{\sigma}{\gamma(\gamma_1 + \gamma_2)} e^{ip}$, and the corresponding effective potential may be found. For a given set of parameters, the effective potential thus becomes a function of the angles θ_j, and we can determine what choice of angles minimizes the effective potential. We return to an analysis of the potential landscape in Section 5.5, where we predict the angles θ_j by finding the minima of the effective potential and compare the prediction to the results of a simulation with $\rho = 0$ (see Fig. 5.7). A similar approach has been successfully applied in other contexts [39, 40] in which the system of PDEs is not a gradient system but the system of amplitude equations derived from the PDEs near the onset of a pattern is.

5.5 Numerical Simulations

In this section, we compare our analytical results with numerical simulations of the original system of partial differential equations, Eqs. (5.6) and (5.7). For all simulations, the initial conditions are low-amplitude white noise. We employ a Fourier spectral method with periodic boundary conditions and a fourth-order exponential time differencing Runge-Kutta method for the time stepping as the numerical technique [41, 42]. The spatial grid is 256×256 unless otherwise noted.

As predicted by the amplitude equation analysis, for $\rho < 0$ and b slightly less than b_T, a pattern with stripes parallel to either the x- or y-axis forms for $\gamma_1 < |\gamma_2|$ (Fig. 5.3 (a)), whereas a square pattern aligned with the x- and y-axes forms for $\gamma_1 > |\gamma_2|$ (Fig. 5.3 (c)). Figs. 5.3 (b) and (d) show

a histograms of the surface gradients $\nabla u = (u_x, u_y)$ for the patterns shown in Figs. 5.3 (a) and (c) respectively. In both cases, the histogram has strong peaks. In the case of the square pattern, the peaks are at the four corners of a square, indicating that the pattern is composed of faceted pyramids with nearly flat faces. The ripples are faceted as well since there are two peaks on the u_y axis that are equidistant from the origin.
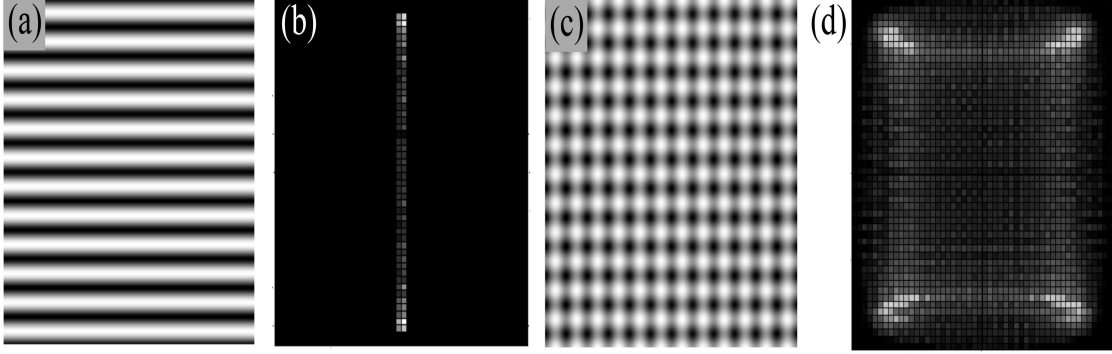
Figure 5.3: (a) and (c): Gray-scale plots of $u(x, y, t)$ at time $t = 20000$ resulting from numerical simulations of Eqs. (5.6) and (5.7) for $a = 0.25$ and $c = 1$ in Region I. For both simulations, $\rho = -0.25$, $\lambda = -1$, $\nu = 1$, and $\eta = 10$. For panel (a), $\alpha_1 = 0.5$, $\alpha_2 = 0.5$, $\beta_1 = 1$, and $\beta_2 = 1$, whereas for panel (c), $\alpha_1 = 0.5$, $\alpha_2 = 0.5$, $\beta_1 = 0.25$, and $\beta_2 = 0.25$. For both plots, the domain is $-60 \leq x, y \leq 60$. For these parameter values, $\gamma_1 = 5.493$. In addition, $\gamma_2 = 14.236$ for panel (a), whereas $\gamma_2 = 4.486$ for panel (c). (b) and (d): Histograms of (u_x, u_y) for the surfaces in panel (a) and (c) respectively. The domain is $-0.9 \leq u_x, u_y \leq 0.9$ for (b) and $-0.8 \leq u_x, u_y \leq 0.8$ for (d).

In Fig. (5.4), we show the time-evolution of the pattern for the particular case $\alpha_2 = \beta_2 = 0$ discussed in Section 5.4. For the chosen parameters, $\beta_1 > -\frac{2}{3}\xi$, and, as predicted by the analysis, the steady-state pattern consists of ripples if $\alpha_1 < \frac{4}{3}\beta_1 + \xi$ (so that $\gamma_1 < |\gamma_2|$), as in Fig. 5.4 (c), whereas the steady state pattern consists of squares if $\alpha_1 > \frac{4}{3}\beta_1 + \xi$ (so that $\gamma_1 > |\gamma_2|$), as in Fig. 5.4 (f). Note that in Figs. 5.4 (a)-(c) the pattern evolves to ripples through states in which there are patches of squares.

The simulations shown in Fig. 5.5 show that even if $\rho \neq 0$, terms arising from the Ehrlich-Schwoebel barrier are necessary if a well-ordered pattern of squares is to form. If there is no ES barrier (so that $\alpha_1 = \alpha_2 = \beta_1 = \beta_2 = 0$), a pattern of rolls forms if the coefficients λ and ν of the quadratic terms in the equations of motion are zero (Fig. 5.5 (a)). As illustrated in Fig. 5.5 (b,c),
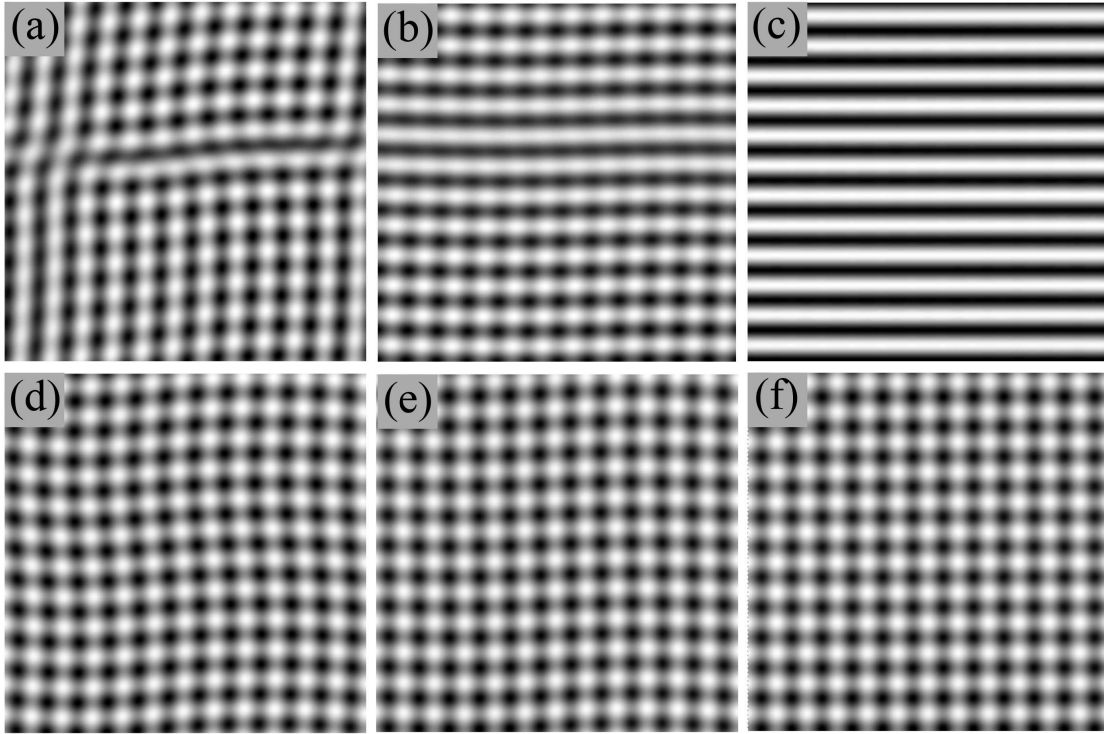
Figure 5.4: Gray-scale plots of $u(x, y, t)$ resulting from two numerical simulations of Eqs. (5.6) and (5.7). Each row is a time series of a simulation. For each simulation, $a = 0.25$, $c = 1$, $\rho = -0.25$, $\lambda = 0$, $\nu = 0$, and $\eta = 10$. For the top row, $\alpha_1 = 0.25$, $\alpha_2 = 0$, $\beta_1 = 0.25$, and $\beta_2 = 0$, whereas for the bottom row, $\alpha_1 = 0.6$, $\alpha_2 = 0$, $\beta_1 = 0.25$, and $\beta_2 = 0$. For these parameter values, $\gamma_2 = 2.486$. In addition, $\gamma_1 = 1.555$ for the top row, whereas $\gamma_1 = 2.868$ for the bottom row. For all plots, the domain is $-60 \leq x, y \leq 60$. The times are (a) 2000, (b) 5000, (c) 10000 for the simulation of the top row, and (d) 2000, (e) 3000, (f) 10000 for the simulation of the bottom row.

the effect of nonzero quadratic coefficients is to produce a pattern which has more resemblance to squares for b closer to the critical value b_T ($b = 0.99b_T$ for Fig. 5.5 (b), whereas $b = 0.96b_T$ for Fig. 5.5 (c)). In both cases, however, the patterns display little order.
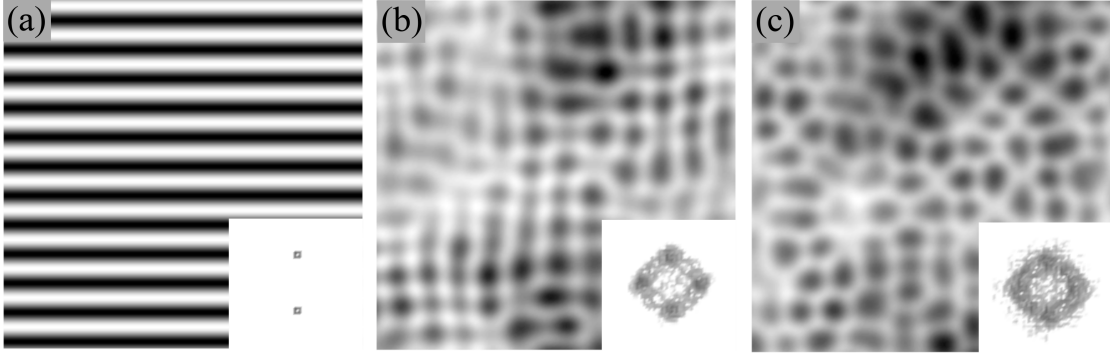
Figure 5.5: Gray-scale plots of $u(x,y,t)$ resulting from numerical simulations of Eqs. (5.6) and (5.7). For each simulation, $a = 0.25$, $c = 1$, $\rho = -0.25$, $\nu = 0$, and $\eta = 10$, $\alpha_1 = \alpha_2 = \beta_1 = \beta_2 = 0$, and the time is $t = 30,000$. For panels (a) and (b), $b = 0.99b_T$, whereas for panel (c), $b = 0.96b_T$. For panel (a), $\lambda = 0$, whereas for panels (b) and (c), $\lambda = -0.5$. For all plots, the domain is $-60 \leq x, y \leq 60$. Insets show the Fourier transform on the domain $-12 \leq k_x, k_y \leq 12$.

The simulations shown in Fig. 5.6 further illustrate the impact of quadratic nonlinearities on the pattern. The coefficients in the amplitude equations (5.22) and (5.23) do not depend on the coefficients λ and ν of the quadratic terms in the equations of motion. In the case in which $\rho = 0$ and there is no Ehrlich-Schwoebel barrier (so that $\alpha_1 = \beta_1 = \alpha_2 = \beta_2 = 0$), our results in Refs. [22] and [23] predict hexagonal patterns in Region I for large enough magnitudes of λ or ν. In the simulations pictured in Fig. 5.6, we select parameters that would give a hexagonal pattern, except that we choose $\rho < 0$, fix $\beta_1 = \beta_2 = 0.25$ and vary $\alpha_1 = \alpha_2$. Our amplitude equation analysis predicts a square pattern for large enough $\alpha_1 = \alpha_2$, and our simulations confirm this prediction. However, the pattern is only well ordered for large enough $\alpha_1 = \alpha_2$. This provides additional evidence that Ehrlich-Schwoebel coefficients of sufficient magnitude are essential for the formation of well-ordered square patterns.

As discussed in Sec. 5.3, for $\rho = 0$, it is not apparent from linear stability analysis that the pattern will be aligned with the x or y axes or that the chosen wavevectors $k_1 = (\cos(\theta_1), \sin(\theta_1))$
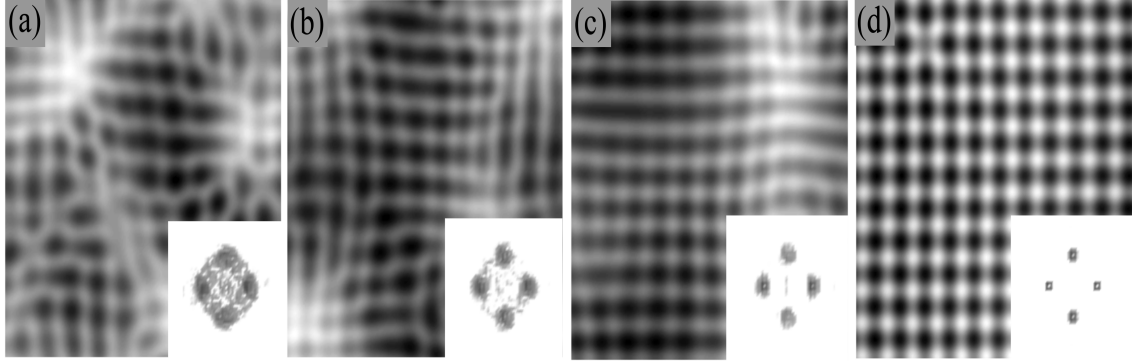
Figure 5.6: Gray-scale plots of $u(x, y, t)$ at time $t = 30000$ with parameters $a = 0.25$ and $c = 1$ chosen from Region I. The remaining parameter values are $\rho = -0.5$, $b = 0.99b_T$, $\lambda = -1$, $\nu = 0$, $\eta = 10$, $\beta_1 = 0.25$, $\beta_2 = 0.25$, and (a) $\alpha_1 = \alpha_2 = 0.5$, (b) $\alpha_1 = \alpha_2 = 1$, (c) $\alpha_1 = \alpha_2 = 1.5$, (d) $\alpha_1 = \alpha_2 = 2$. The domain is $-60 \leq x, y \leq 60$. Insets show the Fourier transform on the domain $-10 \leq k_x, k_y \leq 10$.

and $\mathbf{k}_2 = (\cos(\theta_2), \sin(\theta_2))$ will be orthogonal. In Fig. 5.7 (d), we plot the effective potential (5.33) as a function of θ_1 and θ_2. The effective potential has minima at $(\theta_1, \theta_2) = (\pi/2, 0)$ and $(0, \pi/2)$ and at equivalent choices of (θ_1, θ_2) that correspond to a square pattern aligned with the coordinate axes. In accordance with this prediction, in the time series shown in Fig. 5.7 (a)-(c) for $\rho = 0$ and $\gamma_1 > |\gamma_2|$, the system system evolves to a pattern of patches of squares that are aligned with the coordinate axes.
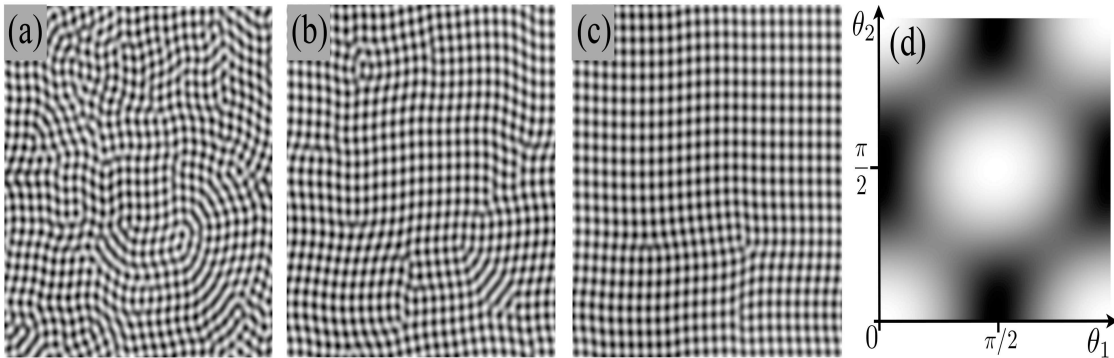
Figure 5.7: (a)-(c) A time series of gray-scale plots of $u(x, y, t)$ with $a = 0.25$ and $c = 1$ chosen in Region I, and $\rho = 0$, $b = 0.96b_T$, $\lambda = 0$, $\nu = 0$, $\eta = 10$, $\alpha_1 = 1$, $\alpha_2 = 0$, $\beta_1 = 0.25$, and $\beta_2 = 0$. The times are (a) 1000, (b) 4000, (c) 18000, and the spatial domain is $-150 \leq x, y \leq 150$. The spatial grid for the simulation is 512×512. (d) A gray-scale plot of the effective potential (5.33) for the values of the parameters in the simulation of panels (a)-(c) as a function of θ_1 and θ_2. Darker shading indicates a lower value of the effective potential.

Our weakly nonlinear analysis and resulting amplitude equations are not applicable for parameter values a and c in Region II. We explore this regime with numerical simulations, as given in Figs. 5.8 and 5.9 for $\rho < 0$ and in Fig. 5.10 for $\rho = 0$. If $\rho < 0$, the pattern coarsens and evolves into either patches of ripples aligned with the axes (Fig. 5.8) if $\gamma_1 < |\gamma_2|$ or a square pattern of ever-increasing length scale if $\gamma_1 > |\gamma_2|$ (Fig. 5.9). The pattern also coarsens in the case $\rho = 0$, as shown in Fig. 5.10.
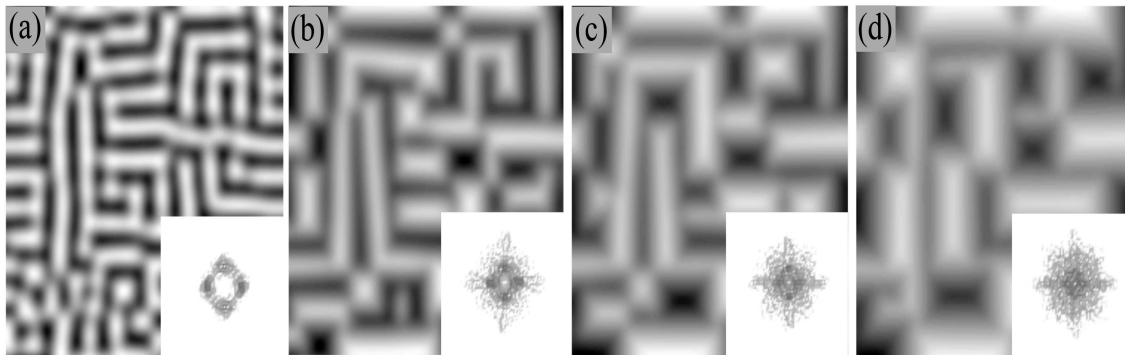
Figure 5.8: A time series of gray-scale plots of $u(x, y, t)$ with parameters $a = 0.75$ and $c = 0.5$ chosen from Region II. The remaining parameter values are $\rho = -0.25$, $b = 0.94a$, $\lambda = 0$, $\nu = 0$, $\eta = 10$, $\alpha_1 = 0.25$, $\alpha_2 = 0$, $\beta_1 = 1$, and $\beta_2 = 0$. The times are (a) 4000, (b) 14000, (c) 30000, (d) 60000, (e) 80000, (f) 100000, and the domain is $-120 \leq x, y \leq 120$. Insets show the Fourier transform on the domain $-30 \leq k_x, k_y \leq 30$.

5.6 Conclusions and Discussion

We have advanced a theory for the spontaneous pattern formation that occurs on the (001) surface of a crystalline binary material with fourfold rotational symmetry about the z axis when it is subjected to normal-incidence ion bombardment. The theory accounts for the Ehrlich-Schwoebel barrier which produces uphill atomic currents and results in cubic nonlinearities involving spatial derivatives of the field u, the deviation from a homogeneous surface height.

As for the case of irradiation of an amorphous binary material, the coupling between u and the surface composition ϕ is key to the formation of well-ordered patterns since it leads to a region of parameter space in which there is a narrow band of unstable wavelengths. Linear stability
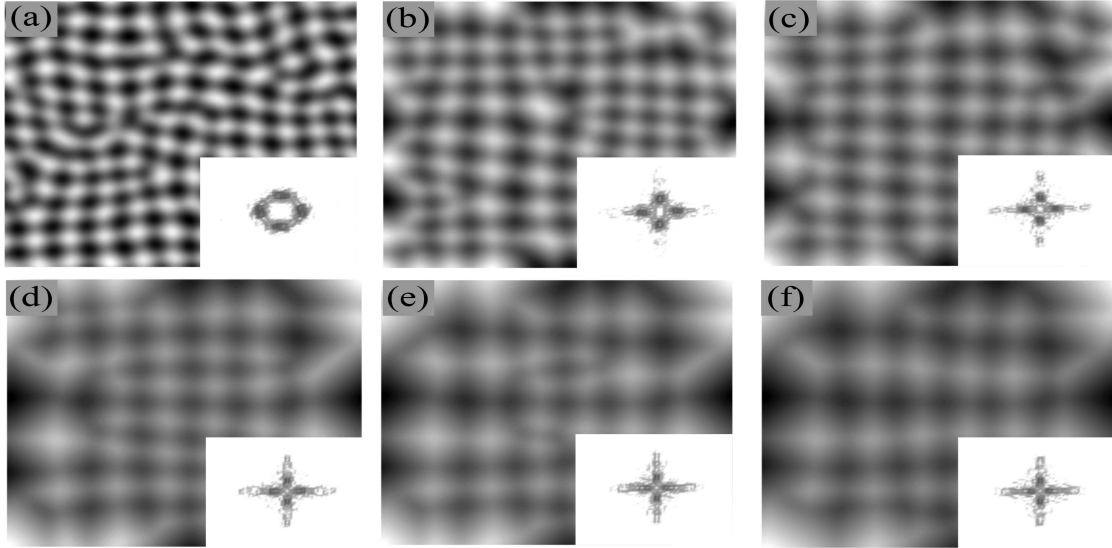
Figure 5.9: A time series of gray-scale plots of $u(x, y, t)$ with parameters $a = 0.75$ and $c = 0.5$ chosen from Region II. The remaining parameter values are $\rho = -0.25$, $b = 0.94a$, $\lambda = 0$, $\nu = 0$, $\eta = 10$, $\alpha_1 = 1$, $\alpha_2 = 0$, $\beta_1 = 0.25$, and $\beta_2 = 0$. The times are (a) 4000, (b) 14000, (c) 30000, (d) 60000, (e) 80000, (f) 100000, and the domain is $-120 \leq x, y \leq 120$. Insets show the Fourier transform on the domain $-30 \leq k_x, k_y \leq 30$.
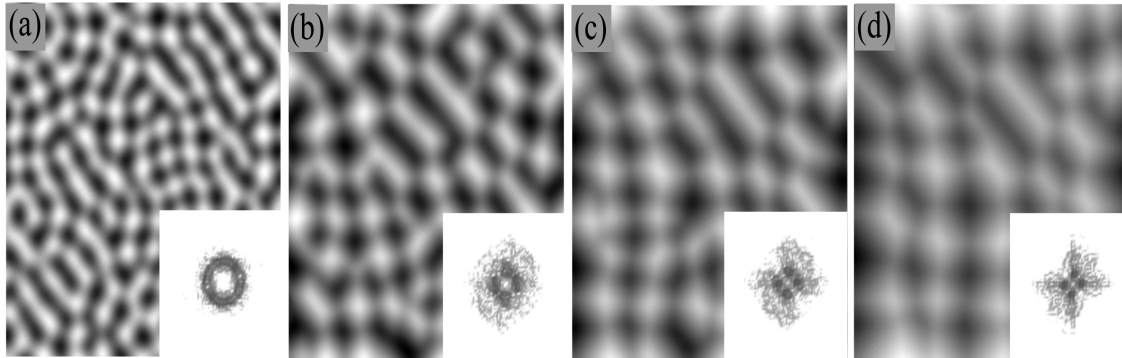
Figure 5.10: A time series of gray-scale plots of $u(x, y, t)$ with parameters $a = 0.75$ and $c = 0.5$ chosen from Region II. The remaining parameter values are $\rho = 0$, $b = 0.94a$, $\lambda = 0$, $\nu = 0$, $\eta = 10$, $\alpha_1 = 1$, $\alpha_2 = 0$, $\beta_1 = 0.25$, and $\beta_2 = 0$. The times are (a) 4000, (b) 14000, (c) 30000, (d) 60000, (e) 80000, (f) 100000, and the domain is $-120 \leq x, y \leq 120$. Insets show the Fourier transform on the domain $-30 \leq k_x, k_y \leq 30$.

analysis shows that if the parameters a and c are chosen so that $a < c$ and $4a > (1 - c)^2$ if $c < 1$, then there is a narrow band of unstable wavelengths. Weakly nonlinear analysis of the model in this region of parameter space and near the critical value of the bifurcation parameter b results in a system of ordinary differential equations for the amplitudes of the Fourier modes. Analysis of these amplitude equations predicts that if the coefficients of the cubic nonlinearities that describe the Ehrlich-Schwoebel barrier are large enough, and the coefficients of those terms obey certain relations (which roughly say that the coefficients α_1 and α_2 of the derivatives with respect to only one variable need to be sufficiently large compared to the coefficients β_1 and β_2 of the terms involving mixed derivatives), then highly ordered square arrays of nanopyramids can form. If the coefficients of the Ehrlich-Schwoebel barrier terms do not satisfy these conditions, then the analysis predicts the formation of well-ordered ripple patterns. These analytical results are supported by numerical simulations of the equations of motion. Histograms of the gradient of u have peaks at the four corners of a square for square array patterns and at either end of a pole for ripple patterns. The square arrays and ripple patterns produced in the presence of the Ehrlich-Schwoebel barrier therefore differ from those produced without this effect.

Cubic nonlinearities in the governing equations are essential for the formation of square arrays since these terms give rise to the cubic terms in the amplitude equations produced by the weakly nonlinear analysis. However, cubic nonlinearities of a very special form are needed for stable square patterns to develop [43]. The cubic nonlinearities that arise from an Ehrlich-Schwoebel barrier lead to solutions in which exactly four Fourier modes have nonzero amplitudes. For the square patterns to be stable, however, the coefficients γ_1 and γ_2 of the cubic nonlinearities in the amplitude equations must satisfy the condition $\gamma_1 > |\gamma_2|$. This condition is not satisfied by a simple cubic nonlinearity such as the term $\eta\phi^3$ that appears in the Bradley-Shipman theory.

Another key requirement for the formation of a well-ordered square array of nanopyramids is that the coefficients λ and ν of the quadratic terms in the governing equations be sufficiently small. As we have shown in previous work, these terms are responsible for the formation of hexagonal arrays of nanodots in the case in which there is no Ehrlich-Schwoebel barrier [22–24]. Even if

the conditions for a square pattern rather than a ripple pattern are satisfied, the quadratic terms can prevent the formation of well-ordered square arrays. For large enough values of the coefficients of the Ehrlich-Schwoebel barrier terms, however, well-ordered square arrays can occur even if the coefficients of the quadratic terms are nonzero.

The parameter ρ in our equations of motion is nonzero if the surface diffusion is anisotropic. For $\rho < 0$ and the bifurcation parameter b close to threshold, the wavevectors for which the real part of the linear growth rate, $\mathrm{Re}\,\sigma_+(\boldsymbol{k})$, is positive are confined to four small regions in wavevector space about each of the orthogonal pairs of wavevectors $\pm\boldsymbol{k}_1 = \pm(k_T, 0)$ and $\pm\boldsymbol{k}_2 = \pm(0, k_T)$. In this case, the square arrays are aligned with the coordinate axes. In contrast, if $\rho = 0$, there is an annulus of wavevectors in which $\mathrm{Re}\,\sigma_+(\boldsymbol{k}) > 0$, and so it not immediately apparent which pairs of wavevectors will be chosen by the dynamics. We obtained a prediction for the chosen wavevectors by finding the wavevectors that minimize the effective potential for the amplitude equations. This prediction is in accord with the results of our simulations. It has also been observed in other contexts, such as convection in a horizontal fluid layer [39] and phyllotactic pattern formation at plant meristems [40], that even for nongradient systems, the amplitude equations may be gradient near threshold and that solutions to the full system of PDEs coincide with minimizers of the effective potential for the amplitude equations.

In contrast to the case in which the parameters a and c are chosen from Region I, linear stability analysis shows that if a and c are chosen from Region II (that is, $a > c$), there is not a narrow band of unstable wavelengths. If $b < a$, then all wavelengths that exceed a critical value are unstable. Numerical explorations of this region in parameter space yield disordered ripple or square patterns that coarsen with time. The square patterns are similar to those produced in the experiments of Ou *et al.* [33] with an elemental crystalline target material. The equation of motion proposed by Ou *et al.* for the case of an elemental material also does not have a narrow band of unstable wavelengths. Although the amplitude equations derived in our weakly nonlinear analysis only apply if there is a narrow band of unstable wavelengths, our simulations suggest that the condition $\gamma_1 > |\gamma_2|$ may nonetheless serve as a guide to producing disordered square arrays if $a > c$.

Our theoretical results provide a strong motivation for experimental studies in which the (001) surfaces of the binary compound semiconductors PbSe, PbS, PbTe and SnTe are subjected to normal-incidence ion bombardment while being maintained at temperatures in excess of their respective recrystallization temperatures. These materials have fourfold rotational symmetry about the z axis. Our results establish that if the experimental parameters are appropriately chosen, highly ordered square arrays of nanoscale pyramids will develop. If successful, these experiments would yield a new entry in the short but growing list of well ordered nanopatterns that can be fabricated by bombardment of a solid surface with a broad ion beam.

5.7 Defect Analysis and Soft Mode in Ion Bombardment of Surfaces

Unrelated to the work of highly ordered square arrays described in Section 5.1-5.6, we are currently analysing the emergence and persistence of defects in ion bombardment systems. In the Bradley-Shipman equations of motion, a hexagonal array is predicted if parameter values are within a certain region. However, defects may arise in the hexagonal lattice if certain parameter values are slightly perturbed. In an effort to identify and classify these defects, we ran over 500 simulations. From our results three scenarios arise,

- No defects in the hexagonal array,

- Temporary defects in the hexagonal array,

- Permanent defects in the hexagonal array.

We are trying to identify indicators within these simulations that help us determine the emerging scenario at an earlier time. However, before we run enough simulations to develop the scenarios, we need to determine parameter values in our system to which the emergence of defects in sensitive.
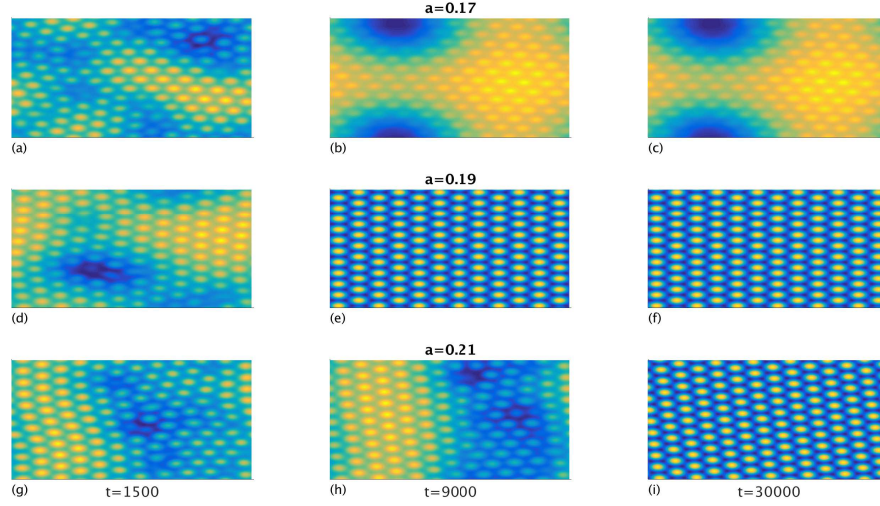
Figure 5.11: For (a)-(i) $\nu = 1.03$ (a)-(c) represent simulations at $a = 0.17$ at time $t =$1500, 9000, 30000 respectively (d)-(f) represent simulations at $a = 0.19$ at time $t =$1500, 9000, 30000 respectively (g)-(i) represent simulations at $a = 0.21$ at time $t =$1500, 9000, 30000 respectively.

In [26], a linear analysis is conducted and a soft mode term similar to Eq.(5.30) is derived. This soft mode term given by Eq. (5.34) is dependent on a few parameters.

$$\frac{dG}{dt} = \frac{2}{a} \sum_{j=1}^{3} \left[\lambda \left(1 - \frac{a}{c}\right) + \frac{2\nu}{a} \left(\frac{c^2 - a^2}{4c^2}\right)^2 \right] |A_j|^2 + \frac{6\eta}{a} \left(\frac{(a+c)(a-c)}{4c^2}\right)^{\frac{3}{2}} Re(A_1 A_2 A_3)$$

(5.34)

As the regularity of a pattern is believed to be a function of Eq. 5.34, we choose ν and a as our varying parameters that affect the hexagonal pattern in our simulations. We want to vary and see how it impacts the pattern formation. As it can be seen in Fig. 5.11, with a constant ν and $a = [0.17, 0.19.0.21]$ we obtain the three scenarios described earlier. In order to understand the emergence and removal of defects, we plot the average height of defects against time. If there are no defects in our hexagonal pattern then the average height of defects is zero.

Fr one simulation with $a = 0.19$, in Fig. 5.12, we can see the corresponding height of defects that correspond to the simulations in Fig. 5.11. Since we have random initial conditions, in Fig. 5.13 we take an average of height defects across multiple simulations. We can clearly see the
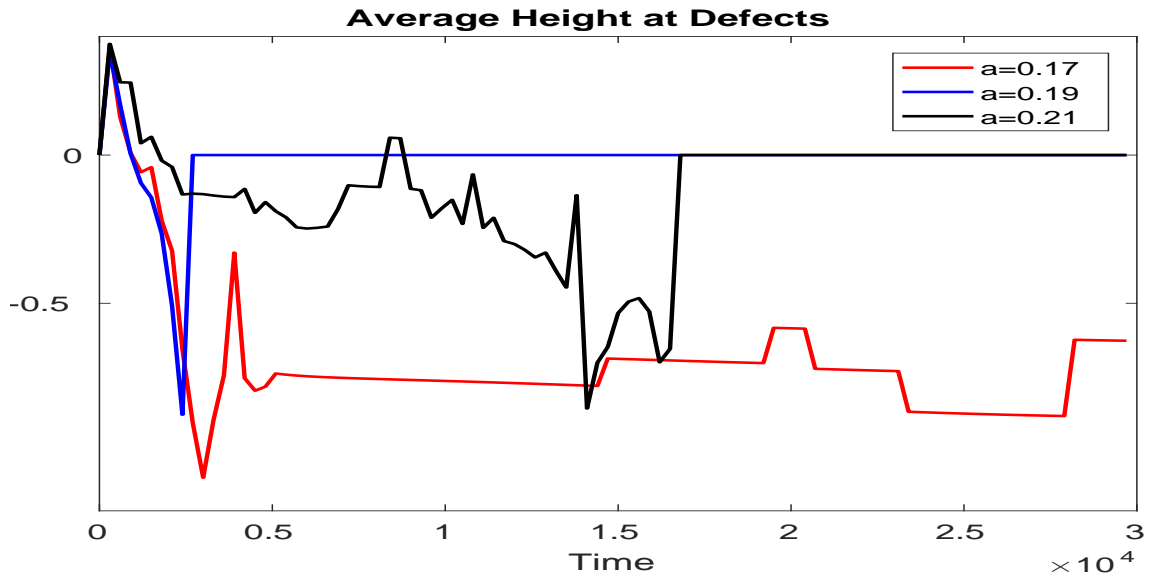
Figure 5.12: Average defect height from one simulation for $a = [0.17, 0.19, 0.21]$.
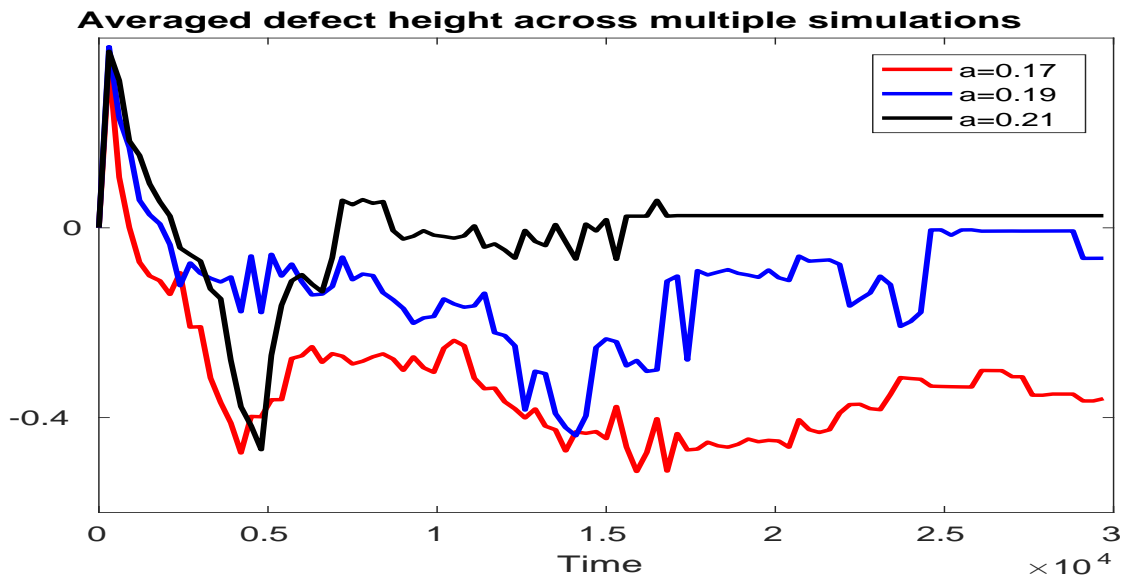
Figure 5.13: Average defect height from multiple simulation for $a = [0.17, 0.19, 0.21]$.

affect of higher softmode on the resulting height of defects. Further work will be to determine these regions where we know more defects develop and when these defects do arise, what are the appropriate steps that might remove them.

Bibliography

[1] T. Lenczycki, *Oscillations in gas-phase periodic precipitation patterns: The NH₃ - HCl Story*. Ms thesis, Colorado State University, Fort Collins, CO, 2003.

[2] B. Hashmi, P. D. Shipman, and R. M. Bradley, "Highly ordered square arrays of nanoscale pyramids produced by ion bombardment of a crystalline binary material," *Phys. Rev. E*, vol. 93, p. 032207, Mar 2016.

[3] A. Einstein, "Über die von der molekularkinetischen Theorie der Wärme geforderte Bewegung von in ruhenden Flüssigkeiten suspendierten Teilchen," *Ann. Phys.*, vol. 322, pp. 549–560, Jan. 1905.

[4] V. Nanjundiah, *Alan Turing and "The Chemical Basis of Morphogenesis"*, pp. 33–44. Tokyo: Springer Japan, 2003.

[5] R. H. Khonsari and V. Calvez, "The origins of concentric demyelination: Self-organization in the human brain," *PLOS ONE*, vol. 2, pp. 1–7, 01 2007.

[6] S. Thompson and P. D. Shipman, "Patterns, oscillations, and microtornadoes: Extreme events in vapor-to-particle reaction zones," *Procedia IUTAM*, vol. 9, pp. 138 – 164, 2013.

[7] C. M. Banic and J. V. Iribarne, "Nucleation of ammonium chloride in the gas phase and the influence of ions," *Journal of Geophysical Research*, vol. 85, pp. No. C 12: 7459–7464, 1980.

[8] C. M. Banic and J. V. Iribarne, "Observation of ion clusters in ion-induced nucleation," *Journal of Aerosol Science*, vol. 17, pp. 95–105, 1986.

[9] C. M. Banic and J. V. Iribame, "Equilibrium constants for clustering of neutral molecules about gaseous ions," *Journal of Chemical Physics*, vol. 83, pp. 6432–6448, 1985.

[10] H. B. Baker, "Influence of moisture on chemical change," *Journal of the Chemical Society*, vol. 65, pp. 611–624, 1894.

[11] R. Cazar, A. Jamka, and F.-M. Tao, "Proton transfer reaction of hydrogen chloride with ammonia: Is it possible in the gas phase?," *Chemical Physics Letters*, vol. 287, pp. 549–552, 1998.

[12] N. W. Howard and A. C. Legon, "Nature, geometry, and binding strenght of the ammonia-hydrogen chloride dimer determined from the rotational spectrum of ammonium chloride vapor," *Journal of Chemical Physics*, vol. 88, pp. 4694–4701, 1988.

[13] A. J. Barnes and A. C. Legon, "Proton transfer in amine-hydrogen halide complexes: comparison of low temperature matrices in the gas phase," *Journal of Molecular Structure*, vol. 448, pp. 101–106, 1998.

[14] E. J. Goodwin, N. W. Howard, and A. C. Legon, "The rotational spectrum of ^{15}n-ammonium chloride vapour: Characterization of the hydrogen-bonded dimer h$_3$n...hcl," *Chemical Physics Letters*, vol. 131, pp. 319–324, 1986.

[15] G. A. Davies, A. B. Ponter, and S. Singh, "The influence of water on the rhythmic process of precipitation of ammonium chloride formed by the counterdiffusion of ammonia and hydrogen chloride," *The Canadian Journal of Chemical Engineering*, vol. 49, no. 1, pp. 71–75, 1971.

[16] G. A. Davies, A. B. Ponter, and S. Singh, "Analysis of the particle size distribution of ammonium chloride formed by rhythmic precipitation of ammonia and hydrogen chloride," *The Journal of Physical Chemistry*, vol. 72, no. 12, pp. 4320–4323, 1968.

[17] R. N. Goh, S. Mesuro, and A. Scheel, "Spatial wavenumber selection in recurrent precipitation," *SIAM Journal on Applied Dynamical Systems*, vol. 10, no. 1, pp. 360–402, 2011.

[18] G. T. Dee, "Patterns produced by precipitation at a moving reaction front," *Phys. Rev. Lett.*, vol. 57, pp. 275–278, Jul 1986.

[19] J. B. Keller and S. I. Rubinow, "Recurrent precipitation and liesegang rings," *The Journal of Chemical Physics*, vol. 74, no. 9, pp. 5000–5007, 1981.

[20] V. B. Shenoy, W. L. Chan, and E. Chason, "Compositionally modulated ripples induced by sputtering of alloy surfaces," *Phys. Rev. Lett.*, vol. 98, p. 256101, Jun 2007.

[21] S. Facsko, T. Dekorsy, C. Koerdt, C. Trappe, H. Kurz, A. Vogt, and H. L. Hartnagel, "Formation of ordered nanoscale semiconductor dots by ion sputtering," *Science*, vol. 285, pp. 1551–1553, 1999.

[22] R. M. Bradley and P. D. Shipman, "Spontaneous pattern formation induced by ion bombardment of binary compounds," *Phys. Rev. Lett.*, vol. 105, p. 145501, Oct 2010.

[23] P. D. Shipman and R. M. Bradley, "Theory of nanoscale pattern formation induced by normal-incidence ion bombardment of binary compounds," *Phys. Rev. B*, vol. 84, p. 085420, Aug 2011.

[24] R. M. Bradley and P. D. Shipman, "A surface layer of altered composition can play a key role in nanoscale pattern formation induced by ion bombardment," *Applied Surface Science*, vol. 258, no. 9, pp. 4161–4170, 2012.

[25] F. C. Motta, P. D. Shipman, and R. M. Bradley, "Highly ordered nanoscale surface ripples produced by ion bombardment of binary compounds," *Journal of Physics D: Applied Physics*, vol. 45, no. 12, p. 122001, 2012.

[26] F. C. Motta, P. D. Shipman, and R. M. Bradley, "Theory of nanoscale pattern formation produced by oblique-incidence ion bombardment of binary compounds," *Phys. Rev. B*, vol. 90, p. 085428, Aug 2014.

[27] S. A. Mollick, D. Ghose, P. D. Shipman, and R. M. Bradley, "Anomalous patterns and nearly defect-free ripples produced by bombarding silicon and germanium with a beam of gold ions," *Applied Physics Letters*, vol. 104, no. 4, p. 043103, 2014.

[28] G. Costantini, S. Rusponi, F. B. de Mongeot, C. Boragno, and U. Valbusa, "Periodic structures induced by normal-incidence sputtering on ag(110) and ag(001): flux and temperature dependence," *Journal of Physics: Condensed Matter*, vol. 13, no. 26, p. 5875, 2001.

[29] A. Levandovsky and L. Golubović, "Epitaxial growth and erosion on (001) crystal surfaces: Far-from-equilibrium transitions, intermediary states, and vertical asymmetry," *Phys. Rev. B*, vol. 69, p. 241402, Jun 2004.

[30] E. Chason and W. L. Chan, *Spontaneous Patterning of Surfaces by Low-Energy Ion Beams*, pp. 53–71. Berlin, Heidelberg: Springer Berlin Heidelberg, 2010.

[31] L. GoluboviÄĞ, A. Levandovsky, and D. Moldovan, "Interface dynamics and far-from-equilibrium phase transitions in multilayer epitaxial growth and erosion on crystal surfaces: Continuum theory insights," *East Asian Journal on Applied Mathematics*, vol. 1, no. 4, p. 297âĂŞ371, 2011.

[32] G. Costantini, F. Buatier de Mongeot, C. Boragno, and U. Valbusa, "Is ion sputtering always a "negative homoepitaxial deposition"?," *Phys. Rev. Lett.*, vol. 86, pp. 838–841, Jan 2001.

[33] X. Ou, A. Keller, M. Helm, J. Fassbender, and S. Facsko, "Reverse epitaxy of ge: Ordered and faceted surface patterns," *Phys. Rev. Lett.*, vol. 111, p. 016101, Jul 2013.

[34] X. Ou, K.-H. Heinig, R. Hubner, J. Grenzer, X. Wang, M. Helm, J. Fassbender, and S. Facsko, "Faceted nanostructure arrays with extreme regularity by self-assembly of vacancies," *Nanoscale*, vol. 7, pp. 18928–18935, 2015.

[35] S. Vogel and S. J. Linz, "Surface structuring by multiple ion beams," *Phys. Rev. B*, vol. 75, p. 085425, Feb 2007.

[36] R. Hoyle, "*Pattern Formation: An Introduction to Methods*," 2007.

[37] M. Cross and H. Greenside, "*Pattern Formation and Dynamics in Nonequilibrium Systems*," 2009.

[38] D. Walgraef, "*Spatio-Temporal Pattern Formation*," 1996.

[39] F. H. Busse, "On the stability of two-dimensional convection in a layer heated from below," *Journal of Mathematics and Physics*, vol. 46, no. 1-4, pp. 140–150, 1967.

[40] M. F. Pennybacker, P. D. Shipman, and A. C. Newell, "Phyllotaxis: Some progress, but a story far from over," *Physica D: Nonlinear Phenomena*, vol. 306, pp. 48 – 81, 2015.

[41] S. Cox and P. Matthews, "Exponential time differencing for stiff systems," *Journal of Computational Physics*, vol. 176, no. 2, pp. 430 – 455, 2002.

[42] R. V. Caster and R. Sassi, "Spectral algorithms for reaction-diffusion systems," *Technical Report*, vol. 99, 2006.

[43] W. Pesch and L. Kramer, "Nonlinear analysis of spatial structures in two-dimensional anisotropic pattern forming systems," *Zeitschrift für Physik B Condensed Matter*, vol. 63, no. 1, pp. 121–130, 1986.